University of Maribor
Faculty of Energy Technology

Journal of ENERGY TECHNOLOGY

Volume 11 / Issue 3
NOVEMBER 2018
www.fe.um.si/en/jet.html

Journal of ENERGY TECHNOLOGY

VOLUME 11 / Issue 3

Revija Journal of Energy Technology (JET) je indeksirana v bazah INSPEC© in Proquest's Technology Research Database.

The Journal of Energy Technology (JET) is indexed and abstracted in database INSPEC© and Proquest's Technology Research Database.

JOURNAL OF ENERGY TECHNOLOGY

Ustanovitelj / FOUNDER

Fakulteta za energetiko, UNIVERZA V MARIBORU /
FACULTY OF ENERGY TECHNOLOGY, UNIVERSITY OF MARIBOR

Izdajatelj / PUBLISHER

Fakulteta za energetiko, UNIVERZA V MARIBORU /
FACULTY OF ENERGY TECHNOLOGY, UNIVERSITY OF MARIBOR

Glavni in odgovorni urednik / EDITOR-IN-CHIEF

Jurij AVSEC

Souredniki / CO-EDITORS

Bruno CVIKL
Miralem HADŽISELIMOVIĆ
Gorazd HREN
Zdravko PRAUNSEIS
Sebastijan SEME
Bojan ŠTUMBERGER
Janez USENIK
Peter VIRTIČ
Ivan ŽAGAR

Uredniški odbor / EDITORIAL BOARD

Dr. Anton BERGANT,
Litostroj Power d.d., Slovenia

Prof. dr. Marinko BARUKČIĆ,
Josip Juraj Strossmayer University of Osijek, Croatia

Prof. dr. Goga CVETKOVSKI,
Ss. Cyril and Methodius University in Skopje, Macedonia

Prof. dr. Nenad CVETKOVIĆ,
University of Nis, Serbia

Zasl. prof. dr. Dali ĐONLAGIĆ,
University of Maribor, Slovenia

Prof. ddr. Denis ĐONLAGIĆ,
University of Maribor, Slovenia

Doc. dr. Brigita FERČEC,
University of Maribor, Slovenia

Prof. dr. Željko HEDERIĆ,
Josip Juraj Strossmayer University of Osijek, Croatia

Prof. dr. Marko JESENIK,
University of Maribor, Slovenia

Prof. dr. Ivan Aleksander KODELI,
Jožef Stefan Institute, Slovenia

Prof. dr. Rebeka KOVAČIČ LUKMAN,
University of Maribor, Slovenia

Prof. dr. Milan MARČIČ,
University of Maribor, Slovenia

Prof. dr. Igor MEDVED,
Slovak University of Technology in Bratislava, Slovakia

Prof. dr. Matej MENCINGER,
University of Maribor, Slovenia

Prof. dr. Greg NATERER,
Memorial University of Newfoundland, Canada

Prof. dr. Enrico NOBILE,
University of Trieste, Italia

Prof. dr. Urška LAVRENČIČ ŠTANGAR,
University of Ljubljana, Slovenia

Doc. dr. Luka SNOJ,
Jožef Stefan Institute, Slovenia

Prof. Simon ŠPACAPAN,
University of Maribor, Slovenia

Prof. dr. Gorazd ŠTUMBERGER,
University of Maribor, Slovenia

Prof. dr. Anton TRNIK,
Constantine the Philosopher University in Nitra, Slovakia

Prof. dr. Zdravko VIRAG,
University of Zagreb, Croatia

Prof. dr. Mykhailo ZAGIRNYAK,
Kremenchuk Mykhailo Ostrohradskyi National University, Ukraine

Prof. dr. Marija ŽIVIĆ,
Josip Juraj Strossmayer University of Osijek, Croatia

Tehnični urednik / TECHNICAL EDITOR

Sonja Novak

Tehnična podpora / TECHNICAL SUPPORT

Tamara BREČKO BOGOVČIČ

Izhajanje revije / PUBLISHING

Revija izhaja štirikrat letno v nakladi 150 izvodov. Članki so dostopni na spletni strani revije - www.fe.um.si/si/jet.html / The journal is published four times a year. Articles are available at the journal's home page - www.fe.um.si/en/jet.html.

Cena posameznega izvoda revije (brez DDV) / Price per issue (VAT not included in price): 50,00 EUR

Informacije o naročninah / Subscription information: http://www.fe.um.si/en/jet/subscriptions.html

Lektoriranje / LANGUAGE EDITING

Terry T. JACKSON

Oblikovanje in tisk / DESIGN AND PRINT

Fotografika, Boštjan Colarič s.p.

Naslovna fotografija / COVER PHOTOGRAPH

Jurij AVSEC

Oblikovanje znaka revije / JOURNAL AND LOGO DESIGN

Andrej PREDIN

Ustanovni urednik / FOUNDING EDITOR

Andrej PREDIN

Izdajanje revije JET finančno podpira Javna agencija za raziskovalno dejavnost Republike Slovenije iz sredstev državnega proračuna iz naslova razpisa za sofinanciranje domačih znanstvenih periodičnih publikacij / The Journal of Energy Technology is co-financed by the Slovenian Research Agency.

Spoštovani bralci revije Journal of energy technology (JET)

Vetrna energija predstavlja enega izmed najbolj zanimivih in okolju prijaznih načinov pridobivanja električne energije s pomočjo obnovljivih virov. Tehnologija pridobivanja - tako horizontalnih, kakor tudi vertikalnih vetrnih turbin, je dobro poznana in se še izboljšuje. Po podatkih iz leta 2017 je bila svetovna proizvodnja električne energije s pomočjo vetrnih turbin 515 GW; vsako leto kapaciteta proizvodnje naraste za približno 10 %. V letu 2017 so s pomočjo vetra pridobili 1120 TWh električne energije, kar predstavlja 4,4 % svetovne proizvodnje električne energije. V mnogih državah predstavlja proizvodnja električne energije s pomočjo vetrnih elektrarn zelo pomemben delež. Tako na primer na Danskem s pomočjo vetrnic pridobijo kar 48 % vse električne energije. Tudi nekatere druge države, kot na primer Litva, Nemčija, Portugalska in Španija, pridobijo na ta način več kot 15 % vse električne energije. Največje vetrnice na svetu so prave velikanke, s premeri rotorjev preko 160 m in z električno močjo blizu 10 MW. V Sloveniji imamo delujoči dve večji vetrnici in manjše, ki delujejo za lastno uporabo tam, kjer je težko napeljati elektroenergetsko omrežje. S pomočjo vodikovih in metanolovih tehnologij bi lahko uporabili vetrnice tudi za ogrevanje in hlajenje poslopij, kakor tudi pridobili energijo potrebno za transport. V prihodnjih letih bi bilo potrebno v Sloveniji bistveno povečati izrabo vetrne energije.

Jurij AVSEC
odgovorni urednik revije JET

Dear Readers of the Journal of Energy Technology (JET)

Wind energy is one of the most interesting and environmentally friendly ways of generating electricity through renewable resources. The technology for the production of both horizontal and vertical wind turbines is still improving. According to data from 2017, the global production of electricity with wind turbines was around 515 GW; production capacity increases by approximately 10% each year. In 2017, wind power generated 1120 TWh of electricity, representing 4.4% of global electricity production. In many countries, electricity generation from wind farms is essential; for example, in Denmark, 48% of all electricity is generated by wind turbines. Some other countries, such as Lithuania, Germany, Portugal, and Spain, acquire more than 15 % of their electricity from the wind. The largest wind turbines in the world are giants with a rotor diameter over 160 m and with an electric power close to 10 MW. In Slovenia, there are two larger wind turbines and smaller ones operating for personal use where it is difficult to install electrical grids; there are far too few of these. On the basis of hydrogen and methanol technologies we could use wind turbines also for heating and cooling of buildings, and to obtain energy for transport. In the coming years, the use of wind power in Slovenia should be significantly increased.

Jurij AVSEC
Editor-in-chief of JET

Table of Contents / Kazalo

Journal of Energy Technology

JET Volume 11 (2018) p.p. 11-25
Issue 3, November 2018
Type of article 1.01
www.fe.um.si/en/jet.html

NUMERICAL OPTIMIZATION OF BRAKE DISCS FOR RAILWAY VEHICLES

NUMERIČNA OPTIMIZACIJA ZAVORNIH DISKOV ZA TIRNA VOZILA

Uroš Grivc[1], Simon Muhič[2,3,✉]

Keywords: Divided brake disc, computational fluid dynamics, brake disc temperature, fluid-structure interaction, finite element analysis

Abstract

In this article, a systematic numerical optimization of brake discs for railway vehicles with computer-aided engineering tools is presented. The main design parameters of brake discs were defined. One-way fluid-structure interaction analysis was performed. Computational fluid dynamics software tools were used to calculate heat transfer coefficients, which were transferred into thermal transient finite element method analysis to predict brake disc temperatures during different braking scenarios. Systematic analysis of defined design parameters was made. With the help of computer-aided engineering and numerical parametric design, it was possible to design and analyse several innovative designs for brake discs, which enables energy and material savings.

✉ Corresponding author: Simon Muhič, University of Novo mesto Faculty of Mechanical Engineering, Na Loko 2, SI-8000 Novo mesto, Slovenia, Tel.: +386 7 393 019, E-mail address: simon.muhic@fs-unm.si

[1] KOVIS d.o.o., Brezina 102, SI-8250 Brežice, Slovenia

[2] University of Novo mesto Faculty of Mechanical Engineering, Na Loko 2, SI-8000 Novo mesto, Slovenia

[3] SIMUTEH s.p., Stična 113, SI-1295 Ivančna Gorica, Slovenia

Povzetek

V članku je prikazana sistematična numerična optimizacija zavornega diska za tirna vozila s pomočjo orodij za računalniško podprt inženiring. Definirani so glavni parametri za načrtovanje zavornega diska. Izvedena je bila analiza enosmerne interakcije stena-tekočina. Orodja za numerično dinamiko tekočin so bila uporabljena za določitev toplotne prestopnosti, ki je bila prenesena v termično simulacijo po metodi končnih elementov za določitev temperature zavornega diska v različnih scenarijih zaviranja. Narejena je bila sistematična analiza vpliva definiranih parametrov načrtovanja zavornega diska. S pomočjo računalniško podprtega inženiringa in parametrične numerične analize smo naredili več inovativnih oblik zavornih diskov, ki istočasno omogočajo prihranke energije in materiala.

1 INTRODUCTION

Brake discs are a critical component found in almost all moving vehicles. Safety and reliability are crucial for braking systems. Several types of brake discs are used in rail vehicles, which are mainly divided into two groups: axle-mounted brake discs and wheel-mounted brake discs. Brake discs are usually made from grey cast iron, nodular cast iron or steel, depending on the loads to which they will be subjected.

The use of brake discs prevents the surface of the rolling wheel itself from braking, which is significantly better for the wheels. This increases the lifespan and reduces stress on the wheels, which are also among the most crucial components in rail vehicles. Divided brake discs were developed to facilitate replacement of the brake discs, making the process less time consuming and less expensive.

Brake discs used for rail freight vehicles are subjected to large fluctuations in temperature and must accumulate and dissipate large amounts of energy due to high thermal and mechanical loads. During braking, lower maximum temperatures and temperature gradients are preferred. These are the main cause of brake disc deformations and stress. The stress caused by temperature gradients is far greater than the stress caused by the braking moment as observed from structural, finite element method (FEM), simulations. At the same time, it is also preferable that ventilation losses due to drag be reduced. Ventilation losses are caused by the rotation of the brake disc in the atmosphere. Air circulation is necessary for dissipating heat into the environment, but high ventilation losses can cause high energy use only for air circulation. Unfortunately, most of these parameters are contradictory. Low ventilation losses while obtaining high thermal dissipation or low temperatures while having low mass are very hard to achieve. This is where design parameters described in this paper come into consideration. With an improved design, material and power savings are possible.

Computer-Aided Engineering (CAE), which covers the extensive use of computer software to assist in engineering tasks and analyses, is increasingly evolving in engineering practice. It includes software for the analysis of solids using the finite element method and software for analyses of computational fluid dynamics (CFD), *[1, 2, 3]*. Current software packages enable studies of coupled physics, known as one or two-way fluid-structure interactions (FSI). The CAE software can also include add-ons to automatically optimize the analysed products, *[4, 5, 6, 7, 8]*. CAE analyses are critical in the development of products for achieving an optimized design of the product in the virtual environment.

As described in *[1]*, CFD and FEM analyses are appropriate for predicting real properties of the brake disc. CFD and FEM simulation setup and loading conditions are described in *[1, 2, 3, 4, 9, 10]*. All these papers describe numerical analysis and comparison with real tests. There is also a numerical comparison of full and ventilated brake discs in *[2].*

2 METHODOLOGY

The main subject of the presented research is an axle-mounted brake disc. There are two of these brake discs mounted per axle of a freight rail vehicle with an axle load of 25 t per axle. The goal of systematic optimization with CAE tools is an improvement of the brake discs efficiency while lowering the mass of the disc. The mass of the brake disc is critical, as a lighter brake disc has less rotational and translational inertia. Lower mass also means smaller production costs because less energy and material are needed for the production of the brake disc.

Figure 1 presents a brake disc cutaway for easier presentation of parameters described in the paper. The initial design of the brake disc before the CAE optimization process is presented in the figure. The brake disc has a width of 170 mm, an outer diameter of 590 mm and the inner diameter of 325 mm and 10 mm of wear material. These dimensions were fixed throughout the optimization. The initial weight of the brake disc assembly was 145 kg. The top speed of the analysed vehicle is 160 km/h.

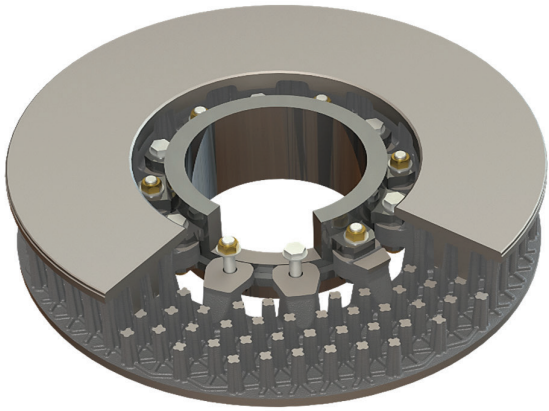

***Figure 1**: Rail freight vehicle brake disc (initial design)*

2.1 Governing equations

The CFD model is solved using the finite volume method with the Reynolds-averaged Navier-Stokes equations (RANS) modelling approach. The computational domain is divided into small volumes where the conservation equations for each volume are integrated. A system of discrete algebraic equations is iteratively solved. The mathematical model used to describe a given physical problem is a set of integral-differential equations and constitutive relations and initial and boundary conditions. Conservation of mass in the general form of the mass conservation equation could be written as *[11]*:

$$\frac{\partial \rho}{\partial t} + \nabla \cdot (\rho \vec{v}) = S_m \tag{2.1}$$

Conservation of momentum is defined with *[11]*:

$$\frac{\partial}{\partial t}(\rho \vec{v}) + \nabla \cdot (\rho \vec{v} \vec{v}) = -\nabla p + \nabla \cdot (\bar{\bar{\tau}}) + \rho \vec{g} + \vec{F} \tag{2.2}$$

Conservation of energy can be defined with *[11]*:

$$\frac{\partial}{\partial t}(\rho E) + \nabla \cdot \left(\vec{v}(\rho E + p)\right) = \nabla \cdot \left(k_{eff} \nabla T - \sum_j H_j J_j + \left(\bar{\bar{\tau}}_{eff} \cdot \vec{v}\right) \right) + S_h \tag{2.3}$$

For transient FEM analysis, the linear system could be defined with *[11]*:

$$[C]\{\dot{T}\} + [K]\{T\} = \{Q(t)\} \tag{2.4}$$

3 DESIGN PARAMETERS AND NUMERICAL MODEL

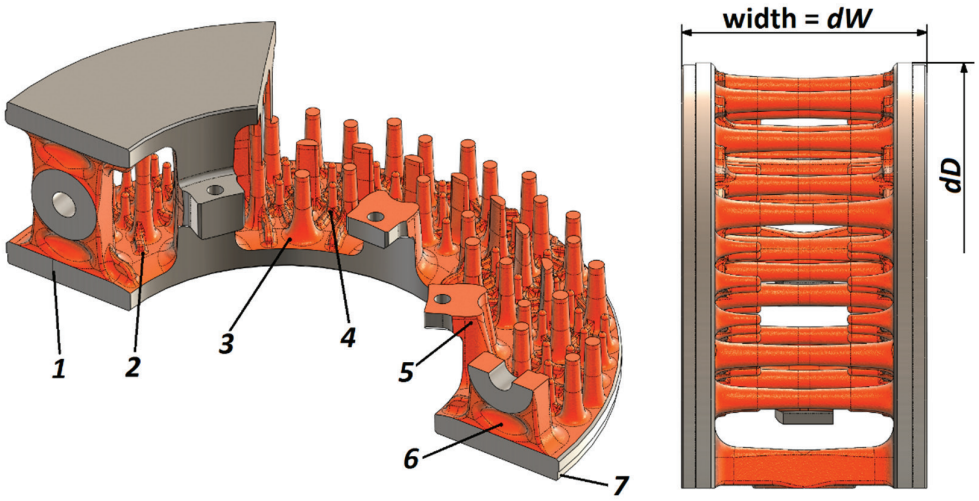

Figure 2: *Presentation of design parameters*

Figure 2 presents the main design parameters of the brake disc, which were varied and studied in the presented research. Some of these parameters, such as dW and dD, are usually fixed by the end-user. Other parameters (1 to 7) could be changed by the designer of the brake disc to achieve the required performance of the brake disc. Parameters 1 to 7, represented in Figure 2 are:

1 Friction plate thickness: it can affect temperatures as heat input is located on it. With increased thickness, lower temperatures are observed as a result of increased thermal capacity. Although high thermal capacity is good, higher plate thickness causes higher mass of the braking plate.

2 Additional net system cooling ribs: it was observed that thermal heat conduction is increased with increasing height and width of these ribs.

3 Radius in the root of the main cooling ribs: it can increase the heat flux from the friction plate towards the centre of the brake disc. The number of ribs itself is a design parameter, but the number must be sufficient to carry the structural loads.

4 Small cooling ribs: they were developed using parametric design optimization. Dimension parameters of cooling ribs are tuned by the use of transient thermal FEM simulation. These small ribs increase the thermal capacity, and they were patented during the design process, because of the large improvement in efficiency. They combine low mass while lowering maximum temperature on the friction surface. These can also be positioned with precision on the spots where they are needed based on transient thermal simulations.

5 The number of mounting brackets: it was observed that maximum stress and deflections are caused by temperature gradients and not by the actual braking torque itself. Phenomena such as thermal banding, hot-spotting and thermal cracking are thought to be the main reasons for disc failure, *[6].* In fact, braking torque of around 8000 Nm per brake disc loads the brake disc only slightly. That is why the number of mounting brackets could be reduced from 12 to 6 as there were some great weight savings made by this reduction. There is another benefit of reducing the number of mounting brackets. That is the increased flow of air through the brake disc, but it caused larger ventilation losses. Some of the cooling ribs are designed for lower air resistance to obtain preferred properties.

6 Some additional weight savings were made by reducing the size of the bracket which connects two halves of the brake disc.

7 Wear limit is presented. It was fixed at 10 mm.

The ANSYS CFX commercial software package was used for CFD simulations. CFD analyses were used mainly to determine wall heat transfer coefficient values and ventilation losses. Previous research proved that prediction of ventilation losses corresponds with real measurements *[1, 9]*. The material of the brake disc is EN-GJL-250 grey cast iron which has a relatively high thermal conductivity of 60 W/(mK), but it has a relatively low density of 7.2 kg/dm^2. There are also other material choices, such as nodular cast iron or CrMo steel, *[7].* The choice of material is based on its mechanical properties, cost, and thermal diffusivity.

Numerical mesh, used for CFD simulations, represents the surrounding air and a rotating domain. Domain size was proven to be large enough not to have any effect on the results. The mesh has fine inflation layers on the walls to capture high-pressure gradients and heat transfer. The domain was decomposed into six subdomains for better control over the mesh, *[1].* The innermost domain was meshed with tetrahedral and other domains with hexahedral elements. By continuous refining of the mesh, we found that the solution, independent of the computational mesh, could be calculated with the mesh with 13.8 million elements.

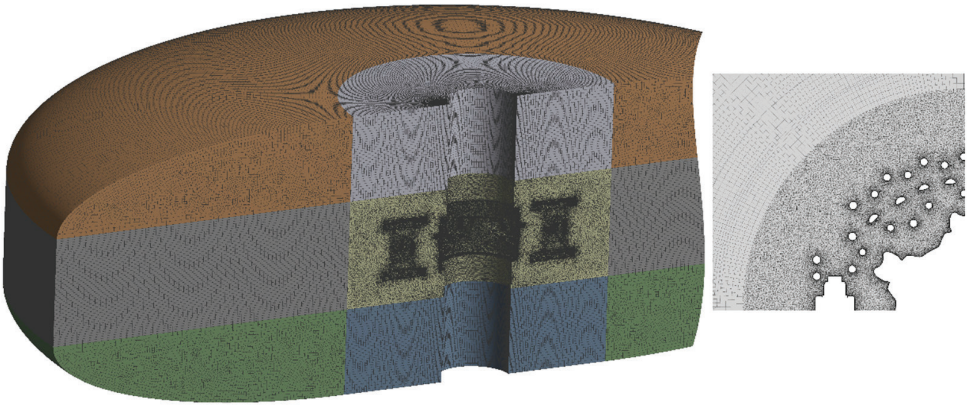

Figure 3: *Numerical mesh for CFD simulation*

Results from CFD simulations were then used as boundary conditions in transient thermal FEM simulations (one-way Fluid-Structure Interaction simulations). Figure 4 presents the heat transfer coefficient (HTC) contour transferred from CFD software for one of the analysed cases. The heat input of 550 kW peak at a braking time of 2 s was set on friction surface where brake pad touches the brake disc for an emergency brake scenario: 89% of the total energy was set to be absorbed by the brake disc, and 11% by the brake pad, *[1].* The total breaking time for the emergency brake scenario was 40 s. The drag brake scenario is a longer type of braking, which is based on constant heat inputs of 20, 30, and 40 kW. This scenario simulates a train braking downhill, maintaining a constant velocity of 70km/h. This braking scenario takes 34 minutes from start to finish in which the velocity of the disc remains constant. Both braking scenarios were simulated on new and worn-out brake discs. The worn-out brake disc model had 10 mm thinner braking plates, which resembled a brake disc that is at the end of its lifecycle and should be changed. Meshes were tested for all cases, and the results are independent of the computational mesh.

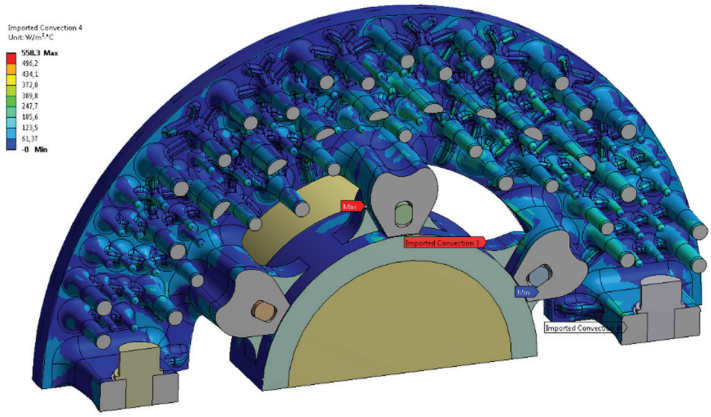

Figure 4: *Model used for transient thermal analyses*

4 PRELIMINARY STUDY OF PARAMETRIC DESIGN STRATEGIES

4.1 Net pattern cooling ribs

Figure 5 represents parametrized net cooling ribs. Net cooling ribs are small ribs that connect larger load-bearing ribs. These are arranged as a net pattern, which explains their name. The temperature chart represents maximum emergency brake temperatures on the friction surface. On the figure, the left-most cooling rib has no net rib. On the right-most cooling rib, the net rib is optimized based on the mass-to-heat flux ratio. The cooling rib had a fixed width, but the height and radius were variables. This simulation was done on a very small subsection, so numerous different designs were analysed.

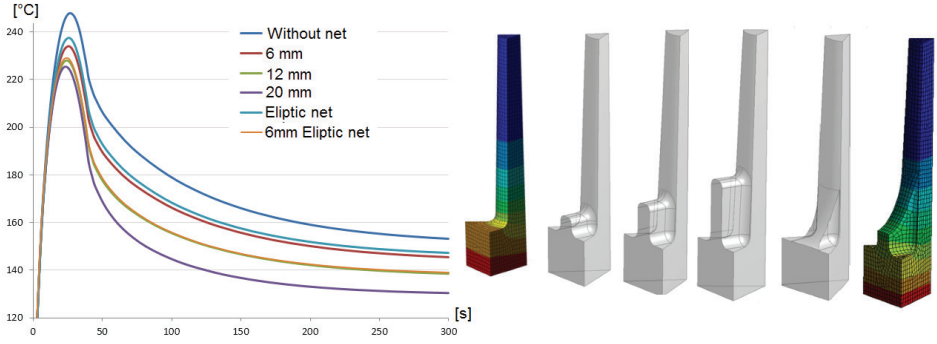

Figure 5: *Net cooling rib design*

It was observed that small intermediate cooling ribs like those presented in Figure 5 could increase heat flow from the friction plate towards the centre of the brake disc. This helps to lower the maximum temperatures given the same power input and material properties.

4.2 Cooling rib height parameter

Figure 6 presents the average and maximum temperatures of the cooling rib during emergency stop braking. It was observed that cooling fin length does not affect temperatures during short, powerful braking scenarios. The difference is negligible because heat does not have enough time to be conducted towards the centre of the brake disc. It is seen that a longer cooling rib has a lower average temperature and stays cooler after the braking is already over.

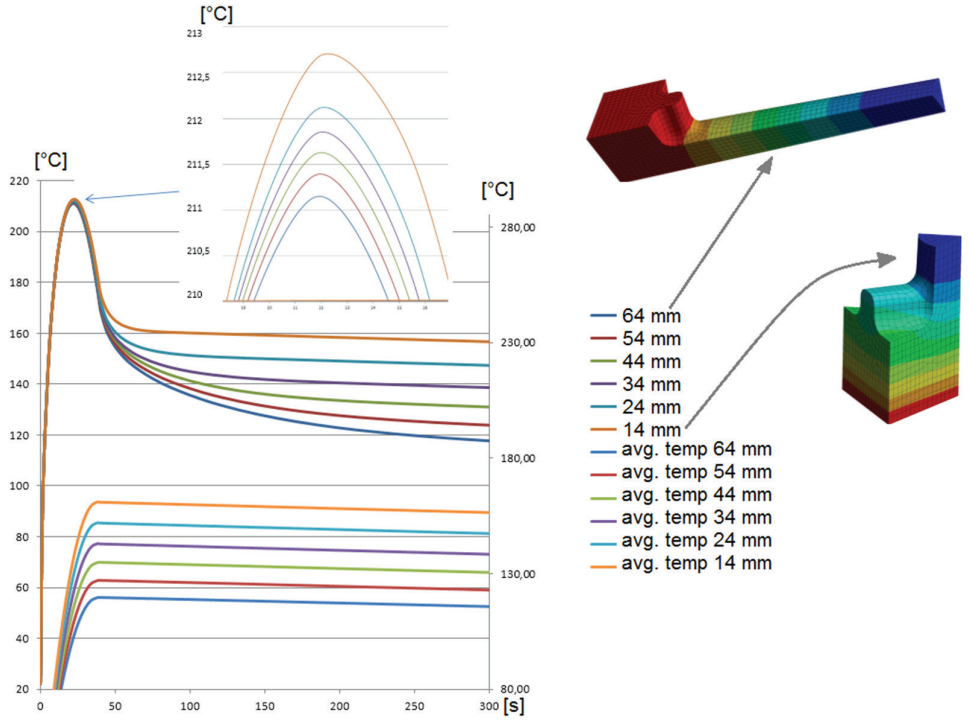

Figure 6: *Height of the cooling fin as a parameter, this parameter corresponds to the width of the disc*

4.3 Root filet of the cooling ribs

The radius in the root of the cooling ribs was set as a parameter. As observed in Figure 7, an elliptic radius was placed in the root of the large cooling ribs. Figure 7 represents four different designs; the left-most model has no radius, and the right-most model has a large radius in the root. All models were simulated in new and worn condition and both for emergency and for drag brake scenarios. The worn condition represents a braking plate thickness that is 10 mm worn away. It was observed that a large root radius of the cooling rib lowers the maximum temperatures of the friction surface during emergency braking. Lower temperatures are desirable, but the use of large fillets makes the weight go up so a compromise must be made.

Lower temperatures are a consequence of area A for the heat conduction increasing, which increases heat flow towards the centre of the brake disc away from the heat input surface.

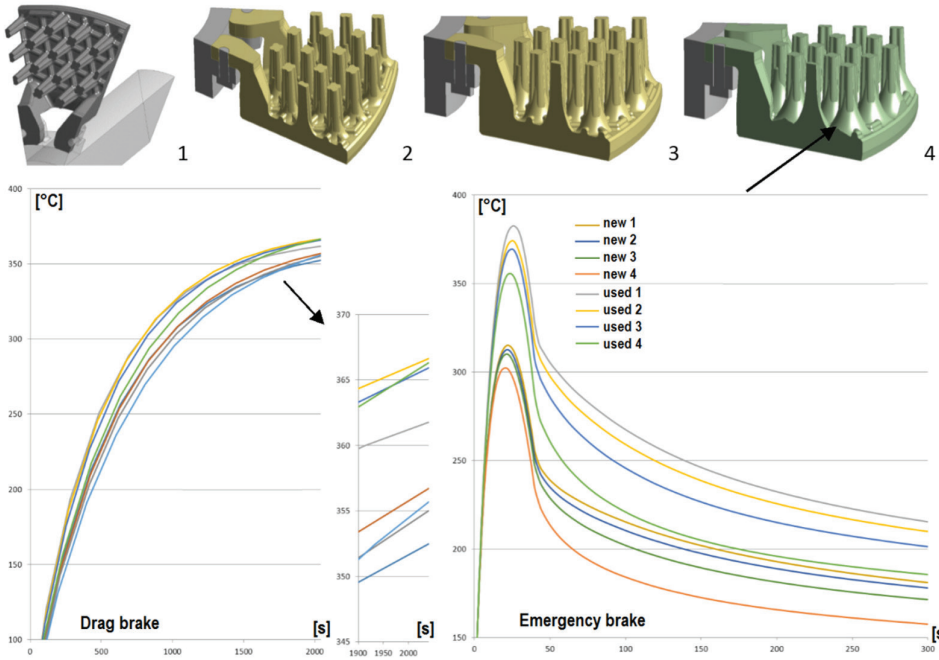

Figure 7: *Root filet parameter*

4.4 Intermediate cooling ribs

It was observed from our previous parametric studies that it is preferred to have the distribution of mass more towards the brake plates where heat input is located. From the structural simulation, it was observed that the number of large load-bearing cooling ribs could be reduced and that the mass could be "moved" more towards the brake plates, so this was examined more closely. Figure 8 represents three designs, although much more designs were tested out. Parameters were, in this case, concentrated more on the intermediate cooling ribs. Effects on temperature during emergency and drag brake were examined. We can conclude that huge difference in maximum temperatures can be made during short breakings with the use of intermediate cooling ribs while reducing mass greatly. These small cooling ribs also have great thermal dissipation properties. Intermediate cooling ribs were isolated, and separate simulations were done to optimize the shape of these ribs, and a patent was made. The optimization was done with the multi-objective genetic algorithm (MOGA) which is a variant of a popular non-dominated sorted genetic algorithm-II (NSGA-II) based on controlled elitism concepts. Figure 9 presents this small rib and its effect on the temperature field. It simulates the larger one in short breakings but heats up more during long braking due to lower thermal capacity.

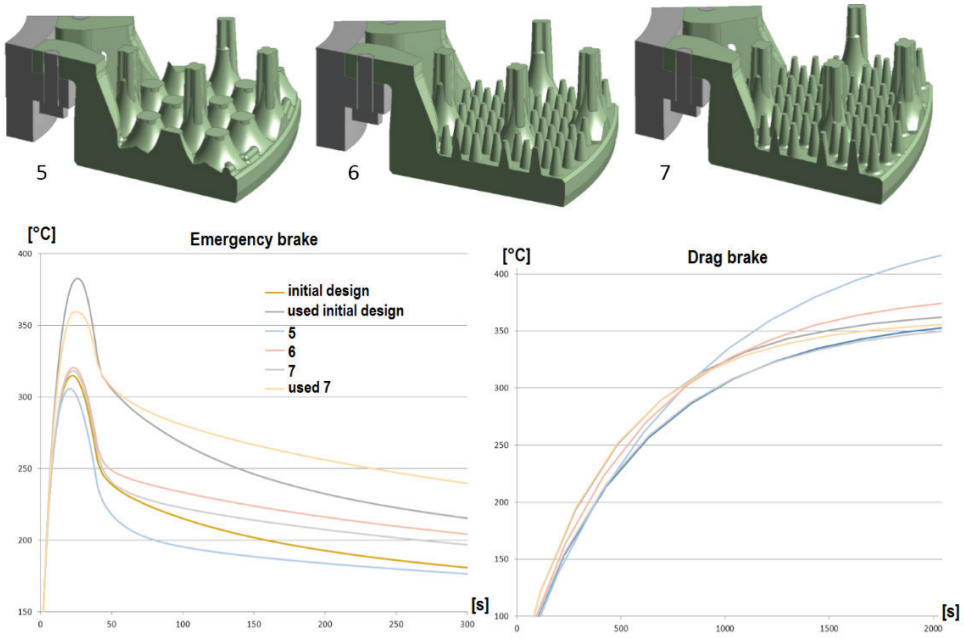

Figure 8: *Number and size of intermediate cooling ribs*

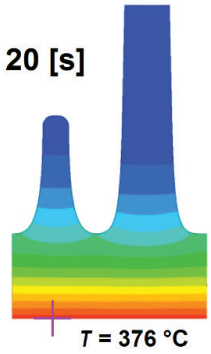

Figure 9: *Optimized intermediate cooling rib during an emergency stop scenario at t = 20 s*

4.5 Cooling rib shape parametric optimization

With the use of computational fluid dynamics software, a simulation was set up so that the cross section of the cooling rib itself was determined by seven parameters. Figure 10 presents how the shape parameters were set. With this type of settings, all the designs from Figure 11 were created automatically. Parameters were varied from a set minimum, and maximum values and a central composite design was used for the design of experiments. About 520 random shapes of cooling rib vents were simulated, with an automatic, intermediate update of geometry.

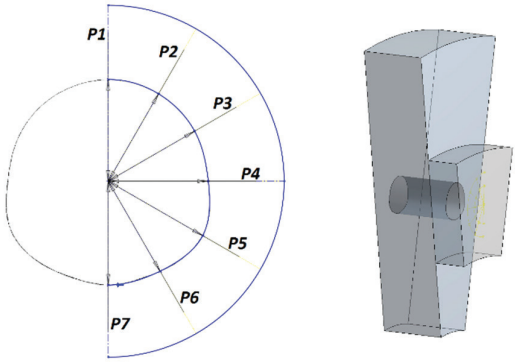

Figure 10: *Cooling rib shape parameters (P1-P7) with a spline used for geometry generation*

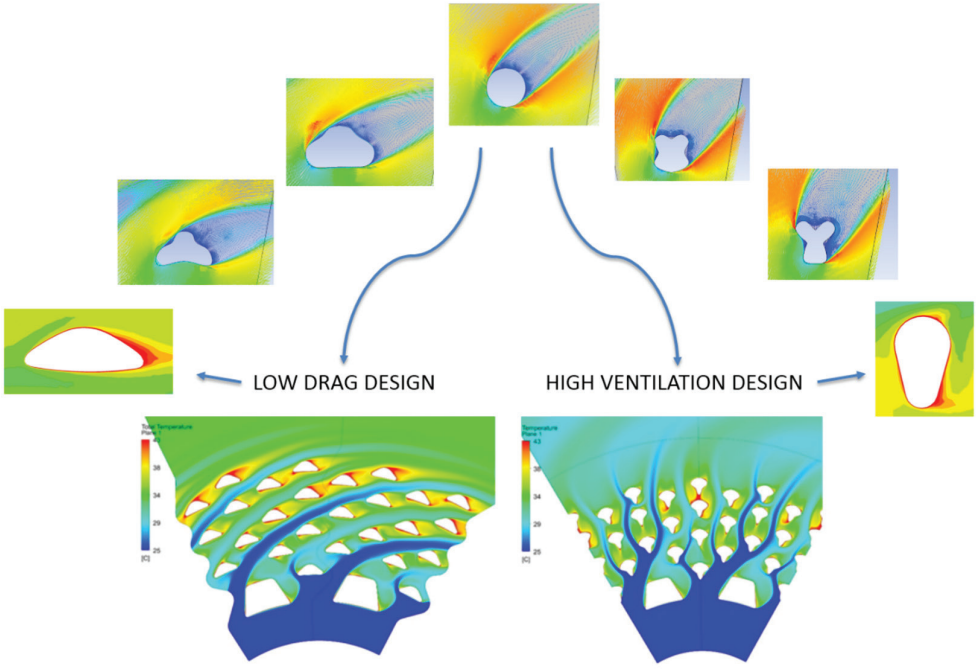

Figure 11: *Parametric optimization of cooling rib*

With results of the systematic disc parameters analysis, it was possible to create and analyse different brake disc designs. Throughout the process, designs were also evaluated to determine whether they were fit for metal casting, as that is the process of making brake discs.

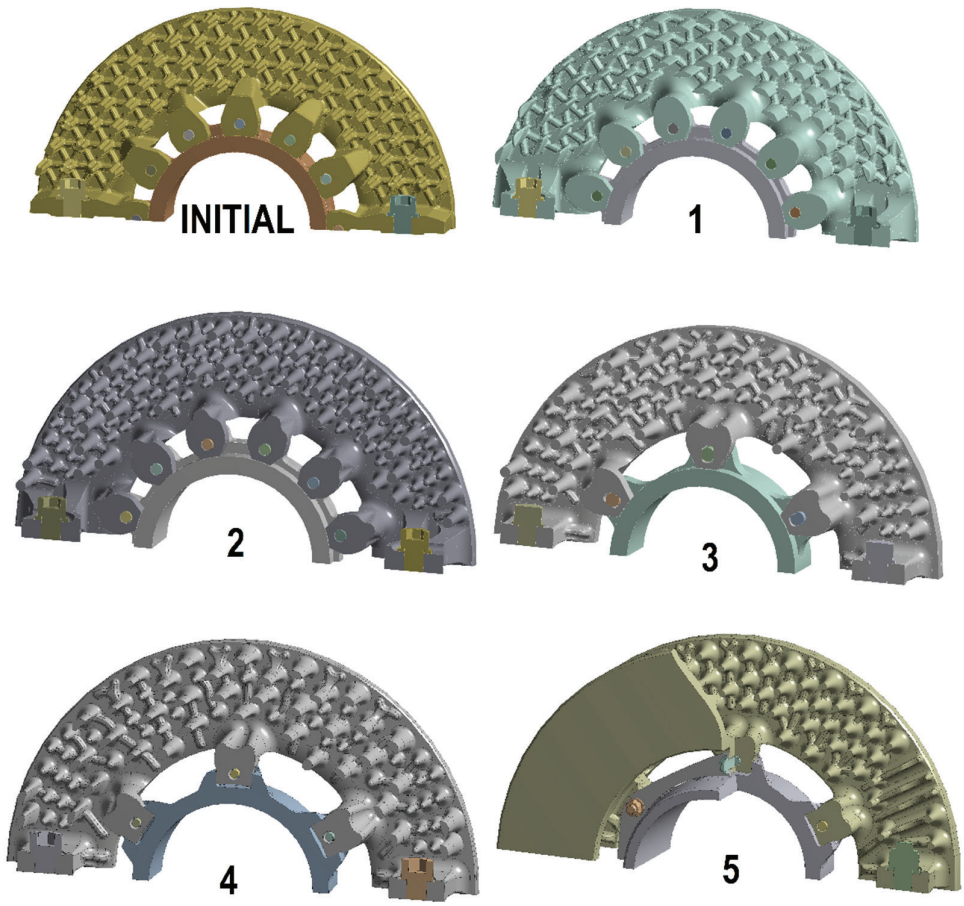

***Figure 12**: Rail Freight vehicle brake disc development*

Figure 12 presents six designs created with the help of parametrical numerical simulations. Brake disc 1 is the initial design of the brake disc. Brake disc 2 is optimized for low ventilation losses. Brake disc 3 is optimized for heat conduction. Brake discs 4 and 6 are optimized for low mass and high thermal dissipation. Brake disc 4 is the best mix of all previous design parameters.

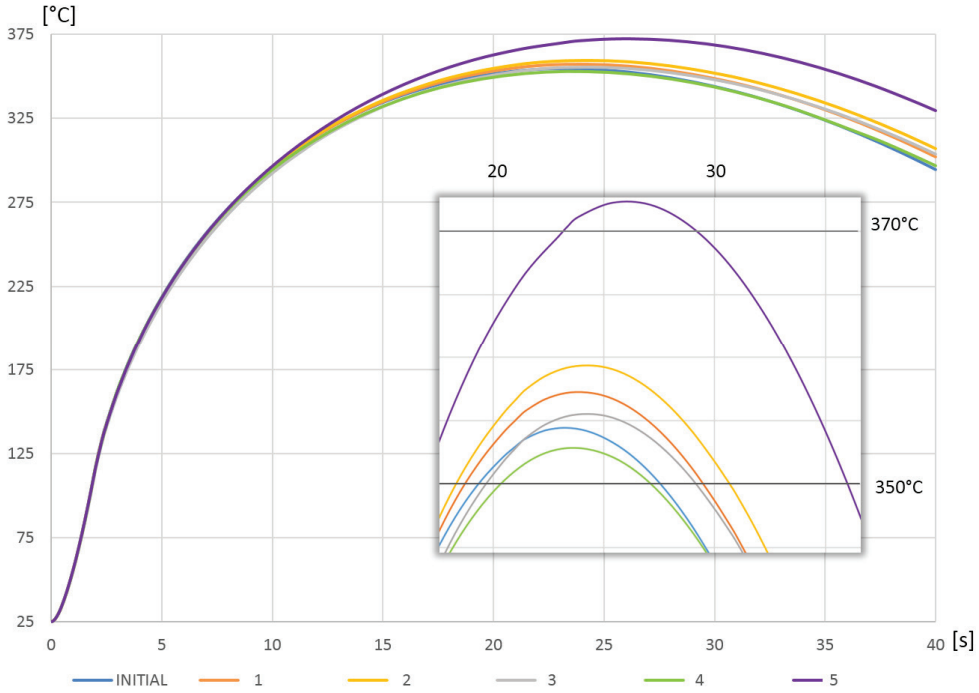

Figure 13: *Emergency brake temperatures of 6 brake disc designs*

Figure 13 shows emergency brake temperatures for six analysed designs of brake discs. As is observed from the chart, the lowest temperature during emergency braking was achieved with Design 4, despite it being 21.4% lighter than initial design and having 21% less ventilation loss. Design 2 has the lowest air resistance. Low ventilation losses also save energy during operation, as there can be around 180 brake discs in a train composition. In this case, if the composition is travelling at 160 km/h, it is possible to reduce the power needed to run it by 36 kW. With the optimized shape of the cooling rib, it is possible to save energy and increase the efficiency of the moving vehicle.

5 CONCLUSION

The performed parametric design analysis again confirmed that, with the use of computational fluid dynamics simulations and structural simulations, using the finite element method, CAE analyses are a very important tool in the development of products. The performed complex study of coupled physics, one-way fluid-structure interaction simulation, was done by systematic parametric optimization, which enables the study of novel ideas and optimized design of the product in the virtual environment.

Parametric design optimization was used at the beginning of the study to optimize the shape of cooling ribs. With newly defined geometry parameters we could change specific properties of brake disc parameters, which are essential during braking, which was confirmed with two types of braking scenarios simulations. It was confirmed that defined design parameters affect

maximum and average temperatures obtained during braking and that optimal brake disc design depends on the loading type.

Based on the parametric study new designs of the braking disc were studied. All new designs are significantly better than the initial design. It was observed that all novel designs achieve lower maximum and average temperatures obtained during an emergency braking scenario, but they are at the same time significantly lighter than the initial design.

It was also observed that all designs have fewer ventilation losses due to the drag of brake disc in a real environment. Low ventilation losses save energy during operation. With the optimized shape of the cooling rib, it is possible to save energy and increase the efficiency of the moving vehicle. With 180 brake discs in a train composition and speed of composition at 160 km/h, it is possible to reduce the energy use by 0.225 kWh/km. In case of electric composition and if emission for electricity production is 315 g CO_2 per kWh [12] we could expect 71 g lower emissions of CO_2 per every km, which could lead to significant reduction of emissions.

References

[1] **U. Grivc:** *Numerical simulation of thermal and structural loads in rolling stock brake disc,* University of Maribor, Faculty of Mechanical Engineering, 2016

[2] **A. Belhocine:** *Computational fluid dynamics modelling and computation of convective heat coefficient transfer for automotive disc brake rotors,* February 2018 Computational Thermal Sciences, vol. 10(1) pp. 1–21, 2018

[3] **M. Reibenschuh, G. Oder, F. Čuš, I. Potrč:** *Modelling and Analysis of thermal and Stress Loads in Train Disc Brakes – braking from 250 km/h to Standstill,* Strojniški vestnik - Journal of Mechanical Engineering, vol. 55(7-8), pp. 494–502, 2009

[4] **P. N. Gunjal:** *Design, Analysis & Optimization of Disc Brak*e, International Engineering Research Journal, Special Issue 2, pp. 5010–5016, 2015

[5] **I. Cayiroglu R. Kilic:** *Wing aerodynamic optimisation by using genetic algorithm and Ansys,* ACTA PHYSICA POLONICA, Vol 132, pp. 981–985, 2017

[6] **A. Durgude, A. Vipradas, S. Kishore, S. Nimse:** *Design optimisation of brake disc geometry,* MAE 598-2016-11, Final Report, 2016

[7] **P. Baskara Sethupathi, A. Muthuvel, N. Prakash, L. Stanly Wilson:** *Numerical Analysis of a Rotor Disc for Optimization of Disc materials,* Journal of Mechanical Engineering and Automation, vol. 5(3B), pp. 5–14, 2015

[8] **E. Palmer, R. Mishra, J. Fieldhouse:** *An optimization study of a multiple-row pin-vented brake disc to promote brake cooling using computational fluid dynamics,* Proceedings of the Institution of Mechanical Engineers Part D Journal of Automobile Engineering, 223(7) pp. 865–875, 2009

[9] **M. Pevec, I. Potrč, G. Bombek, D. Vranesevic:** *Prediction of the cooling factor of a vehicle brake disc and its influence on the results of a thermal numerical simulation,* International Journal of Automotive Technology, Vol. 13(5), pp. 725−733, 2012

[10] **C. Jiguang, G. Fei:** *Temperature field and thermal stress analyses of high-speed train brake disc under pad variations,* The Open Mechanical Engineering Journal, vol. 9, pp. 371–378, 2015

[11] ANSYS CFX Solver Theory Guide (2016), Release 17.2, ANSYS Inc, Canonsburg

[12] **International Energy Agency:** *CO_2 emissions from fuel combustion*, Highlights, 2017

Funding

This work was supported by the European Union's Horizon 2020 research and innovation programme under grant agreement No. 700985.

Nomenclature

A	Cross-section area
$[C]$	specific heat matrix
dD	disc diameter
dW	disc width
E	energy
$\vec{F}$	gravitational body force and external body forces
$\vec{g}$	standard gravity vector
J_j	diffusion flux of species *j*
$[K]$	thermal conductivity matrix
k_{eff}	effective conductivity
p	static pressure
$\{Q(t)\}$	time-dependent heat flow rate vector
S_h	volumetric heat sources.
S_m	mass added to the continuous phase
t	time
$\{T\}$	temperature vector
$\{\dot{T}\}$	time derivative vector of temperature
$\vec{v}$	velocity vector
ρ	density of the fluid
ρ_S	density of the solid
$\bar{\bar{\tau}}_{eff}$	stress tensor

Journal of Energy Technology

JET Volume 11 (2018) p.p. 27-35
Issue 3, November 2018
Type of article 1.01
www.fe.um.si/en/jet.html

VISUALIZATION OF ELECTRIC ENERGY PRODUCTION IN POSAVJE IN A MIXED REALITY ENVIRONMENT

VIZUALIZACIJA V POSAVJU PROIZVEDENE ELEKTRIČNE ENERGIJE V OKOLJU MEŠANE RESNIČNOSTI

Jure Jazbinšek[R], Gorazd Hren[1]

Keywords: 3D visualization, electric energy production, Microsoft HoloLens

Abstract

New technologies for visualization enable new possibilities for data visualization. This paper deals with the challenge of presenting the production of electric energy in a specific geographic area for a specific period. Old-fashioned x-y graphs have been surpassed by using holographic mixed reality technology, with the Microsoft HoloLens device. The production of electric energy of multiple power plants was visualized with 3D columns that represent the volume of energy production. 3D columns representing each power plant are correctly scaled to match nominal energy output and dynamically present energy output. Each 3D column is correctly positioned on the heightmap of the Posavje region and gives volumetric visualization of local energy production in the region. Visualization is developed for mixed reality smart-glasses and enables the presentation of energy production anywhere.

Povzetek

Novodobne tehnologije omogočajo nove načine vizualizacije podatkov. Prispevek obravnava izziv za predstavitev proizvodnje električne energije na določenem geografskem območju v določenem

[R] Jure Jazbinšek, ZEL-EN, razvojni center energetike d.o.o., Vrbina 18, 8270 Krško, Tel.: + 386 7 49 10 233, E-mail address: jure.jazbinsek@zel-en.si

[1] Faculty of Energy Technology, Hočevarjev trg 1, Krško

časovnem obdobju. Starodobna vizualizacija z x-y grafi je bila presežena z uporabo holografske mešane realnosti, ki jo omogoča tehnologija Microsoft HoloLens. Proizvodnja električne energije elektrarn v Posavju je vizualizirana v mešani realnosti s 3D stolpci, ki predstavljajo količino proizvedene energije. Velikost 3D stolpcev, ki predstavljajo posamezne elektrarne, je ustrezno prilagojena tako, da ustreza nazivnim močem elektrarn in dinamično predstavljajo proizvedeno energijo v časovnem obdobju. Vsak 3D stolpec je ustrezno umeščen na 3D zemljevidu Posavja in holigramsko prikazuje prostorsko vizualizacijo lokalne proizvodnje energije v regiji. Vizualizacija je razvita in se uporablja za očala mešane realnosti in omogoča predstavitev proizvodnje energije v katerem koli prostoru.

1 INTRODUCTION

How to merge real and virtual worlds has been a subject of debate and research for decades. Futuristic GUIs have been envisioned in science fiction movies, such as *Iron Man* in 2008. The success of the game Pokémon Go makes the potential of augmented and virtual reality in many domains of everyday human life believable. By changing the traditional 3D geographic information carrier from a 2D computer screen perspective to mixed reality glasses using the HoloLens 3D holographic perspective, it changed the traditional vision, body sense, and interaction modes, which enables geographic information systems (GIS) users to experience real 3D GIS. Virtual reality (VR), augmented reality (AR), and mixed reality (MR) headsets are common 3D perspective carriers.

A multitude of papers and studies can be found about different ways of merging reality and virtuality. Many people have heard of the terms 'virtual reality' (VR) and 'augmented reality' (AR). Let us define those terms and discuss taxonomies to understand how they relate.

The most frequently used taxonomy is by Milgram et al., *[1]*, later extended by Ridel, *[2]*, representing the *Reality-Virtuality Continuum* (Figure 1), which is considered to be the primary reference to classify experiences mixing real and virtual environments.

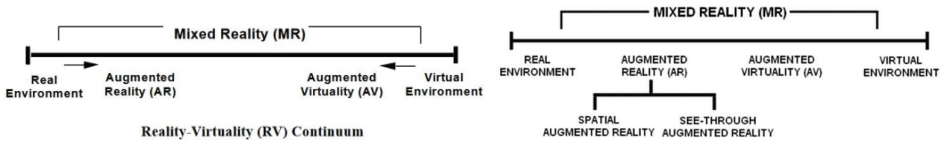

Figure 1: *The original RV continuum by Milgram et al., [1], and the extended version by Ridel, [2]*

Virtual Reality (VR) describes a computer system with which the user is immersed in a three-dimensional virtual world and can interact with it. The usual equipment for VR experiences involves, from head-mounted displays to big screens and CAVE, with a controller (wand, glove) navigating and interacting with the virtual world. In Figure 2, Oculus VR and a recent setup of a corner-CAVE at the Faculty of Energy Technology, University of Maribor, are presented.

Figure 2: *Virtual Reality technology: Oculus VR, [3], and a corner-CAVE.*

Augmented reality (AR) is a type of interactive, reality-based display environment that takes the capabilities of computer-generated display, sound, text and effects to enhance the user's real-world experience. Augmented reality combines real and computer-based scenes and images to deliver a unified but enhanced view of the world, *[4]*.

The simplest types of AR are non-immersive, with which the augmentation occurs on a screen, such as a TV or a smartphone. The display is treated as a window to the augmented world, with many applications in sports broadcasting, for instance (Figure 3). The mentioned Pokémon Go also is an example of monitor-based AR as it takes place on smartphone screens.

Figure 3: *Augmented Reality used at European swimming championships 2018, [5], and Pokémon Go, [6], from Ikea application, [7]*

More complex AR experiences allow the user to see the real world from his own perspective (no screen) via see-through displays augmented with virtual information. Head-mounted displays, (HMDs) known as VR technologies for decades, are nowadays also extensively used in AR. It is possible to project virtual elements on a transparent surface in front of the user, which is called 'optical see-through'; the Microsoft HoloLens is an example of it.

VR places the user in a digital scene with an adequate immersion experience, but it cuts off the physical world. AR presents a real physical world to a user and overlays digital content over it in real time. **Mixed Reality** (MR) requires that the system can correctly handle the relationship between virtual objects and real objects. MR adopts the advantages of both VR and AR. It achieves a symbiotic blend between reality and virtuality. MR results in real and virtual information merged system in real time. MR allows a user to experience depth, spatial persistence, and perspective, while AR cannot, *[10].*

1. 1 MR head-mounted display (Microsoft HoloLens)

To address the problem of accessing 3D geospatial information contention, the MR platform, a typical MR head-mounted display: Microsoft HoloLens (Figure 4), is utilized as an example in this paper to show how to express and visualize 3D geographic information. The Microsoft HoloLens is a pair of 3D perspective holographic glasses with a central processing unit (CPU), a graphics processing unit (GPU) and a holographic processing unit (HPU), *[11].* The HPU is a proprietary chip that handles real-time spatial mapping and processing. The HoloLens has more advanced functions than those of traditional AR devices, including stereoscopic 3D displays, gaze design, gesture design, spatial sound design, and spatial mapping, *[12].*

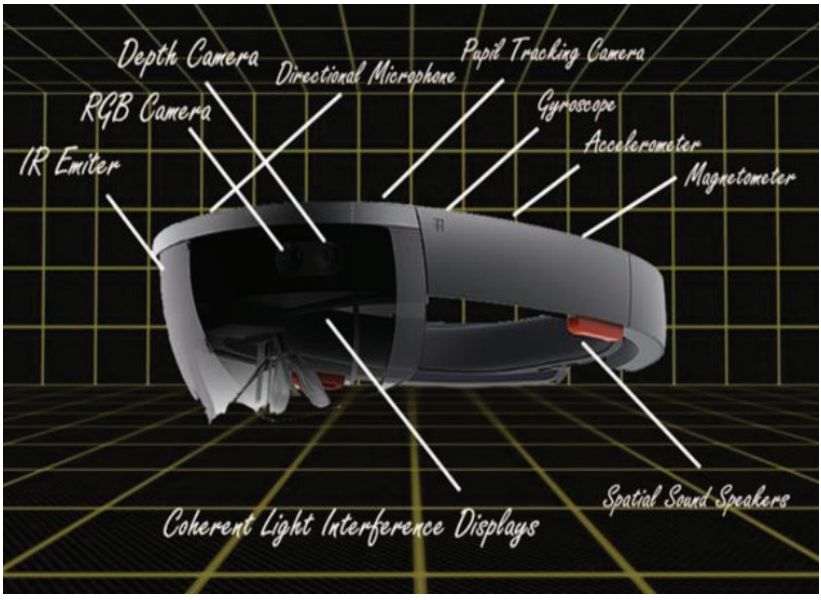

Figure 4: *Microsoft HoloLens [13]*

2 HEIGHTMAP CREATION

A heightmap is a raster image to store surface elevation data and used in displacement mapping to displace the geometric position of points over terrain where the heightmap is converted into a 3D mesh. The geographic scene model is a 3D geographical model that is merged from basic 2D geographic data and height map. The third-party 3D model is a model built on the basis of measured data from multiple power plant electric energy output power.

2. 1 Heightmap Data Source

The heightmap of the Posavje region used as the foundation for the visualization of electric energy was exported from the online tool *TerrainParty*, *[13]*. The extraction of height maps with *TerrainParty* is a straightforward task and gives multiple output files from various sources. It also combines inputs and merges them into a single file.

2. 2 Heightmap Terrain Import

A basis for the visualization of energy production in the game engine *Unity* [16] is the heightmap, which is the foundation map on which data are visualized. The heightmap was exported from *TerrainParty*, from which the appropriate area was selected and exported in *.png* format, as shown in Figure 5.

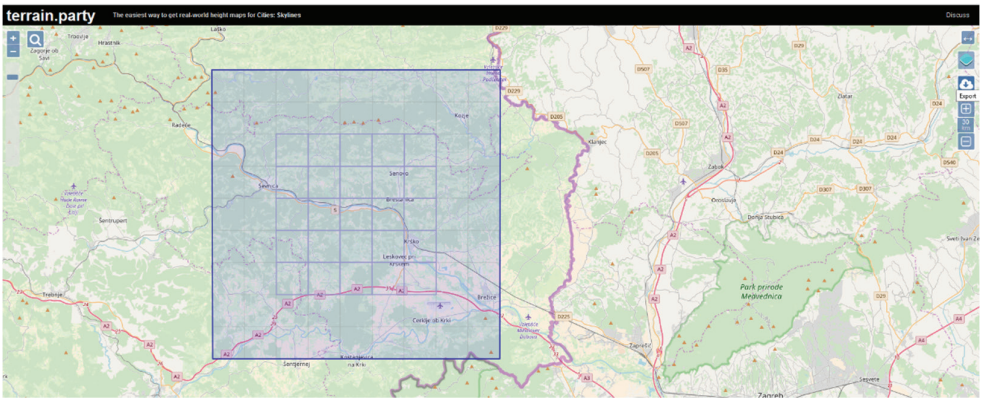

Figure 5: *Export of height map from TerrainParty, [13]*

The heightmap is exported in a condensed format, so it needs to be scaled to the appropriate size, formatted, and imported into *Unity Assets*. To assemble a 3D map, a screenshot image of the Posavje map was also the *Unity* game engine in *Assets*.

To assemble a complete 3D map in the Unity game engine, a *HeightmapFromTexture* script, *[14]*, was used to combine a *Heathtm* map and a screenshot of the Posavje area map. In Unity software, we import the texture of the heightmap obtained from the *terrain.party* and its variable text type (within the *Untiy* texture inspector menu) into an advanced texture.

After changing to the advanced texture, we create a new 3D object in *Unity*, which is determined by the appropriate size. Next, we connect the newly built terrain with the script and the texture by selecting a height folder and the *HeightmapFromTexture* on the *Terrain* to create a 3D object

with the shape of the field. In this way, a basic model is obtained, which is further "normalized" by terrain object and terrain settings. After changing the Terrain Width, Terrain Length, and Terrain Height, Heightmap Resolution is obtained.

The texture of the suitable map with the markings of the places was copied from the map service found at najdi.si, *[15]*. The texture was scaled into the same size to match the size of the generated heightmap from *terrain.party*. The map image has been saved and transferred to Unity. In Unity, the terrain object is selected on the left, in Inspector, "Paint texture" is selected and then "Edit Textures ..." and lastly "Add Texture". The "Add terrain texture" option opens and the texture above and the texture of the Posavje map needs to be selected. Finally, the "size" and "offset" size can be slightly lowered below to fit correctly and the height map, which draws the height of the area.

A view of the hybrid 3D map of Posavje, which is the combination of the black and white height map and texture of map, during implementation phase within the Unity engine, *[16]*, is presented in Figure 6.

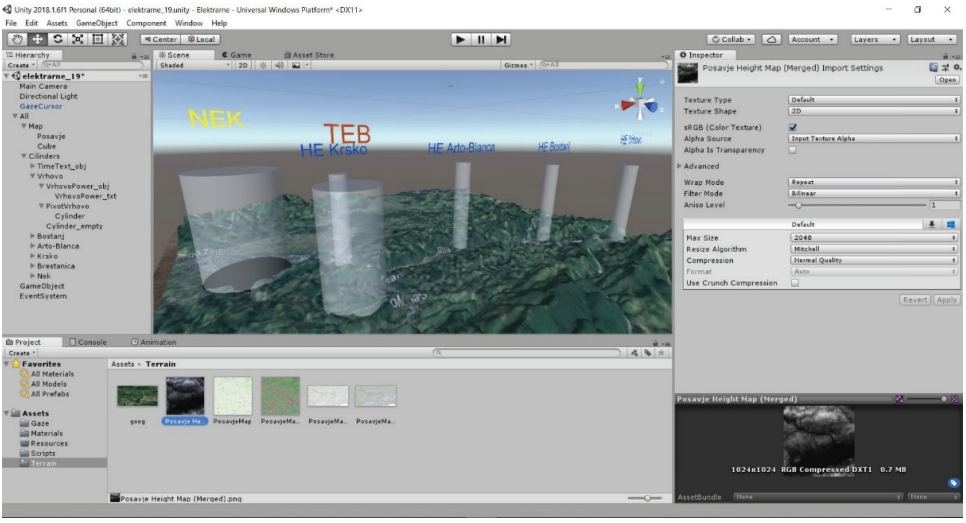

Figure 6: *Implementation of the Posavje 3D map within the Unity engine [16]*

3 DATA TO BE VISUALIZED

From the GEN control centre, the central hub for steering the operation of power generation facilities, data on the operation of power plants were obtained. For the visualization of the production capacities of the power plants in Posavje, the data from the hydroelectric power plants (HPP) of the lower Sava River, the Brestanica Thermal Power Plant (TEB), and the Krško Nuclear Power Plant (NEK), were used and the calculation of ratio between hourly energy output and installed nominal power was performed.

- **HE Vrhovo** with nominal power **34.00 MW**
- **HE Boštanj** with nominal power **32.50 MW**
- **HE Arto-Blanca** with nominal power **39.12 MW**
- **HE Krško** with nominal power **39.12 MW**
- **TEB** with nominal power **114.00 MW**
- **NEK** with nominal power **696.00 MW**

Data on the electricity generation were obtained in MS Excel format (XMS) and exported in CSV format imported into Unity. The data represent the amount of the output power produced in Megawatts (MW) for each hour of the one-week period. The period was selected because the NEK was shut down and restarted during this period. The visualization shows the large energy gradient change that occurs during the one-day outage of the NEK.

Hourly data on the produced output power of the following power plants are presented as coloured 3D columns displayed in holographic mixed reality. Each column represents a specific power plant, where the size of the column ground plan is calculated on the basis of installed output nominal power.

4 VISUALIZATION METHOD

Data energy output from multiple power plants located in Posavje is visualized on a 3D map, which is used for the realistic layout of objects in the space. The produced energy of each power plant is represented by a 3D column (cylinder), whose coloured volume represents the current output power with which the power plant operates. The surface of the ground plan (circle diameter) reflects the total installed power (the sum of all generators) of the power plant. The height of the coloured part of the cylinder shows the current production of the power plant, and for the rated (100%) power for all cylinders is equally high. For a more explicit display, the height of the column is additionally colored with grading between three base colours. If current output power of power plant is 0%, the column is coloured red; the column is coloured yellow at 50% of nominal output and at 100% of output production the column is coloured completely green.

In the Unity engine, all objects (full and empty cylinders) need to be properly defined with the given size, position and dynamic texture of the texture. Optimizing the display of positions and size requires a complex calibration procedure to achieve the appropriate size and layout on the map, as well as the correct inscriptions with the name and power above the cylinder, which illustrates the individual power plant.

The installation and arrangement of cylinders representing various power plants and the implementation of connections between them in the Unity engine is presented in Figure 6.

5 RESULTS OF DATA VISUALIZATION

The reason for the development of an interactive display visualization of electrical energy production is the poor information of the public and visitors of the exhibition about the world of energy. Despite the general knowledge about the type and number of power plants, the average visitor still has no sense of the amount of energy that each power plant produces.

Energy production is visualized by displaying the current power over a certain period, which depends on the installed power, availability, and (in the case of hydropower plants) from natural constraints.

By visualizing the energy production of power plants in Posavje with the help of mixed reality, the developed application designed for Microsoft HoloLens enables spectacularly presenting real data with the latest technology, using hologram techniques.

This paper describes the basic steps for developing energy visualizing application in Unity engine, which allows the user to view visualized data of various power plant production located in Posavje on 3D heightmap on the appropriate locations. The application is useful for displaying the balance of electricity generation and leaves an extremely profound impression on the user, since visualization illustrates the power of each power plant with cylinder volumes that are displayed in the correct ratios. The height of the individual cylinder showing current power reflects the percentage (in %) of the rated power displayed with the empty cylinder (representing nominal installed power 100%) and equally high for all cylinders. The dynamically visualized heights of the cylinders are further coloured to enrich the visualization and further to emphasize the gradient change of energy output.

References

[1] **Milgram P., Takemura H., Utsumi A., Kishinoet F.**, Augmented reality: a class of displays on the reality virtuality continuum., Proceedings of SPIE - The International Society for Optical Engineering 2351, 1994

[2] **Ridel B.**, Interaction techniques, personalized experience and surface reconstruction for spatial augmented reality. PhD thesis. Université de Bordeaux, 2016

[3] https://virtualrealitytimes.com/2015/03/21/nimble-vr-what-it-is-and-what-it-does-for-virtual-reality/ (April 2018)

[4] https://www.techopedia.com/definition/4776/augmented-reality-ar (April 2018)

[5] https://video.eurosport.co.uk/swimming/european-championships/2018/ (April 2018)

[6] https://thenextweb.com/insider/2016/07/20/the-good-the-bad-and-the-really-ugly-of-pokemon-go/ (April 2018)

[7] https://www.wired.com/story/ikea-place-ar-kit-augmented-reality/ (April 2018)

[8] **Wang W., Wu X., Chen G., Chen Z.**, *Holo3DGIS: Leveraging Microsoft HoloLens in 3D, Geographic Information,* International Journal of Geo-Information, MDPI, 7, 60; (www.mdpi.com/2220-9964/7/2/60/pdf), April 2018

[9] **Karthika S., Praveena P. GokilaMani M.,** *Hololens*, International Journal of Computer Science and Mobile Computing, Vol.6 Issue.2, February- 2017, pp. 41-50

[10] **Brigham, T.J.**, *Reality Check: Basics of Augmented, Virtual, and Mixed Reality*, Pages 171-178, Published online: 28 Apr 2017, (https://www.tandfonline.com/doi/full/), May 2018

[11] **Microsoft**, *HoloLens Hardware Details*., accessed on 12 November 2017, (https://developer.microsoft.com/en-

[12] **Furlan, R.** *The future of augmented reality: Hololens-Microsoft's AR headset shines despite rough edges,* IEEE Spectr. 2016, 53, 21. (https://ieeexplore.ieee.org/document/7473143/), April 2018

[13] **TerrainParty**, *Height map extraction tool*, (https://terrain.party/), May 2018

[14] **HeightmapFromTexture**, *Script uses a texture in your project as a heightmap, which is applied to the active terrain* (http://wiki.unity3d.com/index.php/HeightmapFromTexture), June 2018

[15] **Map Texture**, *Screenshot of Posavje map* (zemljevid.najdi.si), June 2018

[16] **Unity**, content-creation engine, https://unity3d.com, March 2018

Nomenclature

GIS	geographic information systems
GUI	Graphical User Interface
HMD	Head mounted display
VR	virtual reality – navidezna resničnost
AR	augmented reality – obogatena resničnost
VR	virtual reality – navidezna resničnost
AR	augmented reality – obogatena resničnost
MR	mixed reality
CPU	central processing unit
GPU	graphics processing unit
HPU	holographic processing unit
TEB	Brestanica Thermal Power Plant
NEK	Krško Nuclear Power Plant
HPP	Hydro-Power Plant
MW	Megawatts

Journal of Energy Technology

JET Volume 11 (2018) p.p. 37-46
Issue 3, November 2018
Type of article 1.01
www.fe.um.si/en/jet.html

A MAGNESIUM-ENHANCED LIME CLEANING PROCESS OF FLUE GASES

PROCES ČIŠČENJA DIMNIH PLINOV Z UPORABO MAGNEZIJSKO OBOGATENE APNENČEVE MOKE

Martin Bricl[✉], Jurij Avsec[1]

Keywords: magnesium-enhanced lime, cleaning of flue gases, thermal power plant, sulphur dioxide.

Abstract

The cleaning of flue gases in thermal power plants has been mandatory since the 1990s in the EU. The most commonly applied process for flue gas cleaning is a wet calcite process that enables the high efficiency of cleaning flue gases with the usage of a reagent that is readily available in nature. This paper presents the process of cleaning the flue gases on a wet basis, but using slaked lime with the content of the magnesium as the reagent. This sort of cleaning process works very well, but the reagent is usually very difficult to find in nature itself.

Povzetek

Čiščenje dimnih plinov v termoenergetskih objektih je prisotno in obvezno v EU že vrsto let. Najbolj razširjen postopek za čiščenje žveplovega dioksida iz dimnih plinov je tako imenovan mokri kalcitni postopek, ki omogoča visoko učinkovitost čiščenja dimnih plinov, z uporabo reagenta, ki je v naravi lahko dostopen – apnenec. Članek predstavlja alternativni postopek čiščenja dimnik plinov, je prav tako moker, a kot reagent uporablja gašeno apno z vsebnostjo magnezija. Uporaba takšnega reagenta v postopku čiščenja dimnih plinov se je izkazala za zelo uspešno, a reagent kot takšen težko najdemo v naravi.

[✉] Corresponding author: Martin Bricl, University of Maribor, Faculty of Energy Technology, Hočevarjev trg 1, SI 8270 Krško, Tel.: +386 51 210 620, Email address: martin.bricl@student.um.si

[1] Jurij Avsec, University of Maribor, Faculty of Energy Technology, Hočevarjev trg 1, SI 8270 Krško, Tel.: +386 7 620 2217, Email address: jurij.avsec@um.si

1 INTRODUCTION

With the combustion of fossil fuels, such as coal and oil, large amounts of sulphur dioxide are emitted into the atmosphere. Sulphur dioxide emissions are well known as having a severe impact on human health and the environment. The major health risks of exposure to high concentrations of sulphur dioxide are breathing difficulties, respiratory illness, and the aggravation of the existing cardiovascular disease. Sulphur dioxide leads to depositions of this harmful substance in the environment, causing serious problems, including the acidification of lakes and streams, and damage to plants, trees and crops. Sulphur dioxide depositions are also responsible for decay and damage on the monuments, buildings, and infrastructure. When particles of sulphur dioxide are in the air (airborne), they might also cause difficulties with visibility.

2 MAGNESIUM-ENHANCED LIME

Magnesium-enhanced lime can be used as the reagent in the desulphurization process of raw flue gases in thermal power plants, where high amounts of the sulphur dioxide are present. Magnesium-enhanced lime is produced as a mixture of slaked lime, which contains calcium hydroxide $Ca(OH)_2$ and magnesium hydroxide $Mg(OH)_2$, *[1]*.

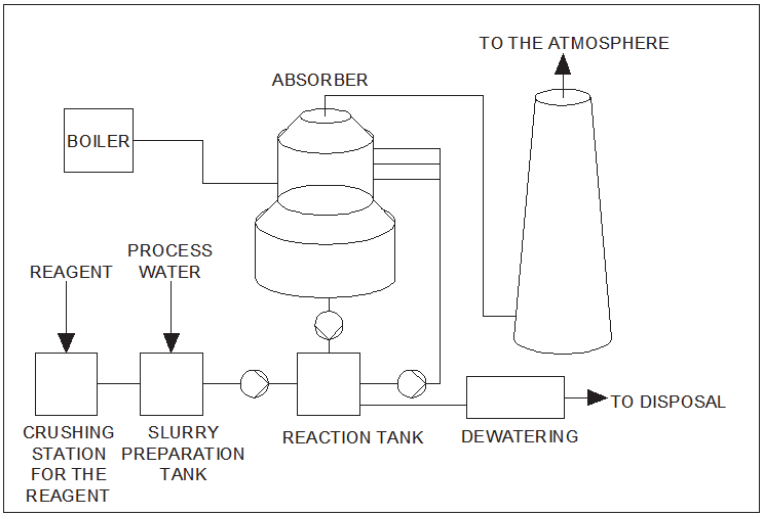

Figure 1: *Desulphurization process with the usage of magnesium-enhanced lime as the primary reagent. The system contains the following main equipment: a crushing station for the reagent, slurry preparation plant, reaction plant, absorber, dewatering station and the wet stack through which the clean flue gases enter the atmosphere.*

The reagent with the proper formation of the two-component mixture is delivered to the absorber into the bottom of it, where pH control is used to replenish the consumed reagent. The fresh slurry is transported from the bottom of the absorber with the assistance of the recirculation pumps to the spraying levels, where the full impact between the flue gases from the boiler unit and the fresh slurry occurs. During the spraying of the slurry on the flue gases that rise

from the inlet towards the outlet of the absorber, the chemical reactions between acid components in flue gases and the neutral components in the fresh slurry happen.

3 MAGNESIUM-ENHANCED LIME & DESULPHURIZATION

Calcium hydroxide in the slurry reacts with most of the acid components, primarily with the sulphur dioxide in the raw flue gases, and the calcium sulphates are formed ($CaSO_3 \bullet 1/2H_2O$). Magnesium hydroxide reacts with the remaining acid components in the flue gases. During this reaction, the soluble magnesium salts (magnesium sulphide $MgSO_3$ and magnesium disulphide $Mg(HSO_3)_2$) are formed.

The presence of the magnesium components in the slurry significantly increases the SO_2 capture and enables the further reduction in the consumed power for the process, the reagent, and the equipment costs. Its presence in the slurry also prevents the pH from sharply decreasing during the operation of the flue gas desulphurization process, which means that this mechanism allows higher and better performance of the flue gas desulphurization process, since there is increased solubility of the sulphur dioxide in the slurry and this consequently means a lower liquid/gas ratio in the absorber.

The presence of the salts that are formed with the help of the magnesium in the slurry prevent the formation of the build-ups on the internal surfaces of the absorber and other essential equipment of the absorber, such as pipes for the recirculation of the slurry or spraying nozzles on the spraying levels.

The primary chemical reactions that occur during the flue gas desulphurization process with magnesium-enhanced lime are shown hereinafter.

$$SO_2 + Ca(OH)_2 \rightarrow CaSO_3 \bullet \tfrac{1}{2} H_2O + \tfrac{1}{2} H_2O \quad (3.1)$$

$$4SO_2 + 3Mg(OH)_2 \rightarrow 2MgSO_3 + Mg(HSO_3) + 2H_2O \quad (3.2)$$

$$CaSO_3 \bullet \tfrac{1}{2} H_2O + \tfrac{1}{2} O_2 + 3/2\ H_2O \rightarrow CaSO_4 \bullet 2H_2O \quad (3.3)$$

$$MgSO_3 + \tfrac{1}{2} O_2 \rightarrow MgSO_4 \quad (3.4)$$

$$Mg(HSO_3) + O_2 \rightarrow MgSO_4 + H_2SO_4 \quad (3.5)$$

The portion of the slurry that is already present in the absorber has reacted with the acid components of the flue gases. The slurry falls from the spraying levels (it is pumped to there from the bottom of the absorber with the assistance of the recirculation pumps) back to the bottom of the absorber. When the pH in the bottom of the absorber reaches the level of 5.5, some of the existing slurry must be extracted from the sump of the absorber. The slurry with mentioned pH level is further pumped to the external forced oxidation tank, where it contacts the air. Calcium sulphite is converted to the gypsum (in crystalline form), magnesium salts are oxidized to the $MgSO_4$ (in solution) as shown in chemical reactions (3) to (5). The slurry is from the external tank transported to the dewatering station, where the by-product of the process is formed (i.e. gypsum in the shape of the cake). The remaining liquid from the dewatering process, still

containing the $MgSO_4$, is transported back to the absorber to help enhance the quality of the slurry and to save the amount of the reagent that is needed for the efficient cleaning of the flue gases.

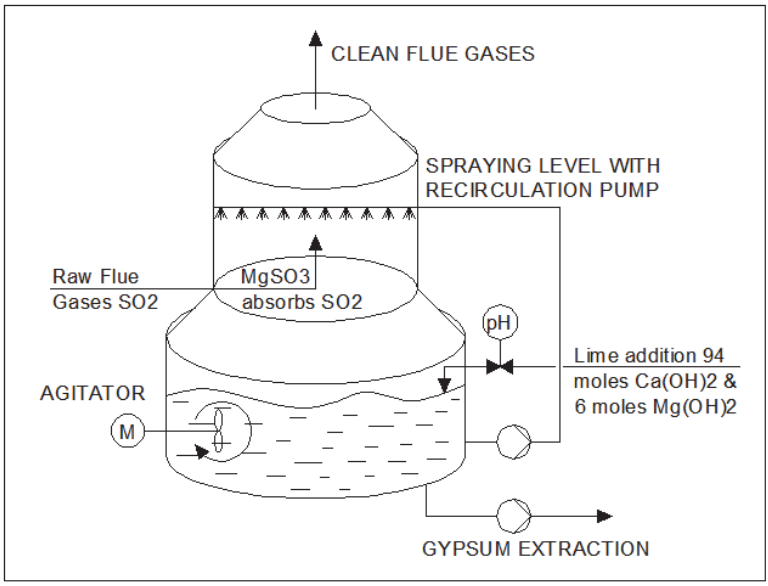

Figure 2: *Magnesium enhanced lime process of cleaning the raw flue gases in the thermal power plant. Raw flue gases and the addition of the fresh lime enter the process, gypsum suspension and clean flue gases exit the process.*

4 NEEDED REAGENT AND BY-PRODUCT OF THE MEL PROCESS

For the preparation of the reagent, calcium oxide and magnesium oxide are needed. The amount of the calcium oxide can be up to 91% by weight, and the amount of the magnesium oxide can be up to 8% by weight. The total amount of the oxides is equivalent to the sulphur dioxide neutralizing value to about 94% CaO.

There are two possibilities for producing the magnesium-enhanced lime: to produce it from limestone with suitable magnesium content, or to blend high-calcium and dolomitic limes (containing approximately 40% MgO).

To properly prepare the reagent for the MEL process, the water must be mixed with the lime in the tank, where the calcium hydroxide and the magnesium hydroxide are formed. The resulting slurry is further added to the lower part of the absorber (i.e. theabsorber recycle tank). The slurry pH 6 is kept in the recycle tank of the absorber to ensure that all of the lime reacts with the sulphur dioxide.

5 SULPHUR DIOXIDE REMOVAL PROCESS RESULTS

In general, we can conclude that the magnesium-enhanced limestone process achieves higher sulphur dioxide removal results than, for example, the traditional wet flue gas desulphurization process that uses lime as the reagent.

The level of efficiency that the MEL process can achieve is between 98% and 99% in thermal power plants that utilize a variety of high- and low-sulphur coals. In the absorber, the liquid-gas ratio is estimated between 40 and 30 to achieve 98% sulphur dioxide removal efficiency.

The MEL desulphurization process can be added to the existing or new thermal power plant blocks, ranging from less than 100MW and up to 1000MW. The sulphur content in coal can be between 2% and 5%, *[2]*, to still achieve the sufficient effect of the desulphurization of the raw flue gases from the boiler.

6 SYSTEM COMPONENTS

6.1 Reagent Handling and Preparation System

Lime is delivered to the site with the transportation truck, after which it is stored in a lime silo. From there, the lime is pneumatically transported to the day silo. With the assistance of the gravimetric feeder, the lime is supplied to the slaking system. When the slurry is ready and mixed, the pumps transport the prepared slurry to the slurry tank. From the fresh slurry tank, the slurry is transported to the absorber recycle tank.

6.2 Sulphur Dioxide Removal System

The primary sulphur dioxide removal process occurs inside the absorber tower. The absorber is a vertical open spray tower in which the counter-current between the upward raw flue gases from the boiler side, and the downward fresh slurry suspension from the spraying levels is achieved, *[3].* Inside the absorber, the primary chemical reactions of absorption of the acid components to the freshly prepared slurry from the spraying levels is happening. When the acid components are removed from the up-stream flue gases, they fall to the bottom of the absorber where they are involved in the process of crystallization and further disposed from the system process to the by-product and handling treatment plant. There, they are properly processed and forwarded to the disposal area or further transported to the consumers of such by-products.

6.3 Flue Gas System with The Stack

The flue gas ducts are intended to lead the raw, untreated flue gases from the boiler exit side to the absorber inlet. Acid protection of the flue gas duct system is not necessarily needed if the flue gases do not condensate and the liquid acid condensate is not in the direct contact with the flue gas ducts. To lead the treated flue gases from the absorber to the atmosphere, we can use the existing chimney of the installation, or we can plan to build the new wet stack. Because of the

absorber and the stack newly attached to the existing installation, the needed draft must be overcome. The additional fan in front of the absorber should usually deliver 170 –2000 Pa, *[4].*

6.4 By-Product Handling and Treatment System

The by-product of the MEL process is gypsum. The used slurry from the absorber is transported from the absorber recycle tank to the dewatering system. With the usage of the vacuum belt filters, we can achieve the dewatered product in the shape of a cake, *[5]*, that can be transported to the covered storage area. From there, it can (if the by-product is of sellable quality) be sold to the offsite user.

7 COST AND PERFORMANCE ANALYSIS OF THE MEL PROCESS

7.1 Cost Comparison Between LFOS and MEL Process

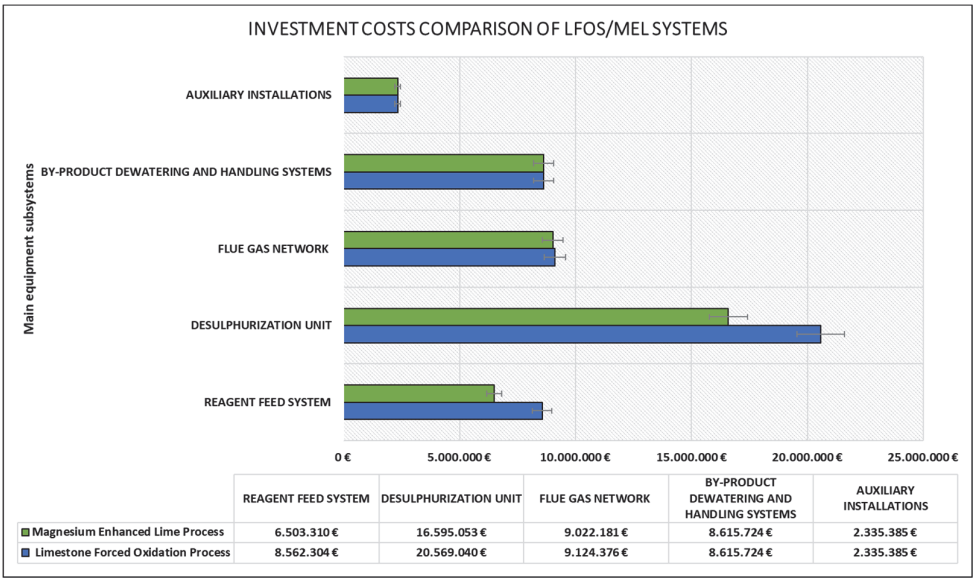

	REAGENT FEED SYSTEM	DESULPHURIZATION UNIT	FLUE GAS NETWORK	BY-PRODUCT DEWATERING AND HANDLING SYSTEMS	AUXILIARY INSTALLATIONS
Magnesium Enhanced Lime Process	6.503.310 €	16.595.053 €	9.022.181 €	8.615.724 €	2.335.385 €
Limestone Forced Oxidation Process	8.562.304 €	20.569.040 €	9.124.376 €	8.615.724 €	2.335.385 €

Figure 3: *The costs comparison of the magnesium-enhanced the lime process, and the limestone forced oxidation process for cleaning of the flue gases in thermal power plants. The magnesium-enhanced lime process requires lower investment costs, but its operational costs can be higher than with the Limestone forced oxidation process.*

The main difference in costs between the two mentioned systems are mainly in initial investment costs and later the variable operational costs. When comparing the investment costs of both systems, it can bee is seen in Figure 3 that the investment costs in flue gas network with ducts, by-product dewatering and handling system and auxiliary installations, are almost at the same level in both systems. The higher investment costs require the limestone forced oxidation system,

since the reagent preparation system cost €2 million and the desulphurization unit is €4 million higher, corresponding to the proposed systems for the magnesium-enhanced lime process.

To analyse the operational costs of the magnesium-enhanced lime-cleaning process, the fixed and variable operational and maintenance costs must be analysed. Hereinafter are described the operational and maintenance costs of such a cleaning unit, expressed as the percentage of the total amount of the operational and the maintenance costs.

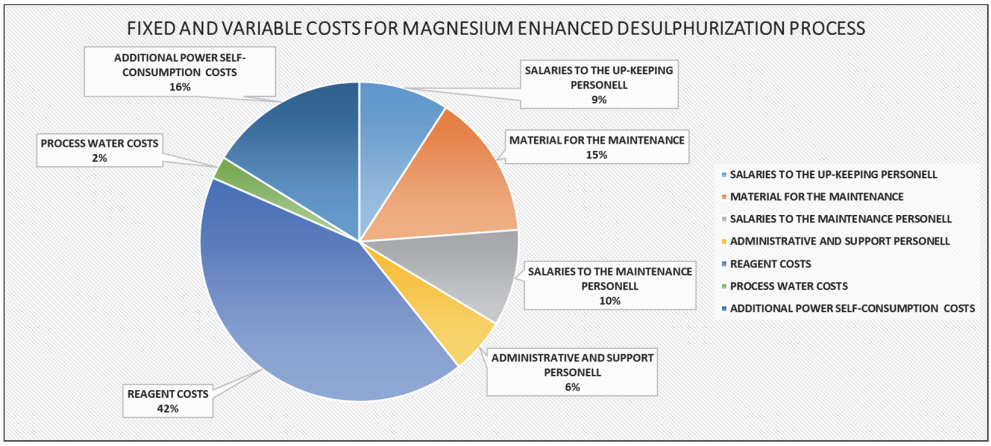

Figure 4: *The pie diagram shows the fixed and variable costs for the magnesium-enhanced desulfurization process, in percentages of the total sum of costs.*

The fixed operational costs of the magnesium-enhanced lime process are mainly the salaries for the maintenance personnel (9%), costs of the material for the maintenance of the flue gas cleaning plant (15%), salaries to the maintenance personnel (10%), and the costs of the administrative and the support personnel (10%).

The variable operational costs are the costs that are dependent on the current price situation on the market, the movement of which dictates the demand and possible supply. Among these costs, we number reagent costs for the chemical reaction to successfully absorb acid components of the untreated flue gases (42%), costs of the process water consumption (2%), and the costs connected with the power self-consumption (16%).

From Figure 4, it is clearly seen that the main cost in operation of the magnesium-enhanced lime desulphurization process is the consumption of the freshly prepared reagent. For that reason, it is sensible to find the location of the lime quarry near the existing thermal power plant; this can reduce the cost of the purchase, delivery and preparation of the reagent.

The power self-consumption of the magnesium-enhanced lime desulphurization process is better than that of the limestone forced oxidation desulphurization process. The reason for that is mainly in the size of the absorption unit, where the primary cleaning of the flue gases is achieved. Because the MEL process uses an enhanced reagent, the reactivity of it is better, and the impact time of the fresh reagent from the spraying level and raw flue gases from the inlet can be shorter, resulting in savings on the expensive anti-corrosion construction materials. Lower construction

of the absorber unit results in fewer spraying levels, which consequently means fewer recirculation pumps and other equipment, which results in the savings of the consumed power or electricity. In Figure 5, the consumption of the electricity for operation of the desulphurization unit of the limestone forced oxidation process (green) and magnesium-enhanced lime process (blue) is presented. Note that for the absorption of the acid components from the raw flue gases, the LFOS process consume almost three times more electricity than the MEL process does.

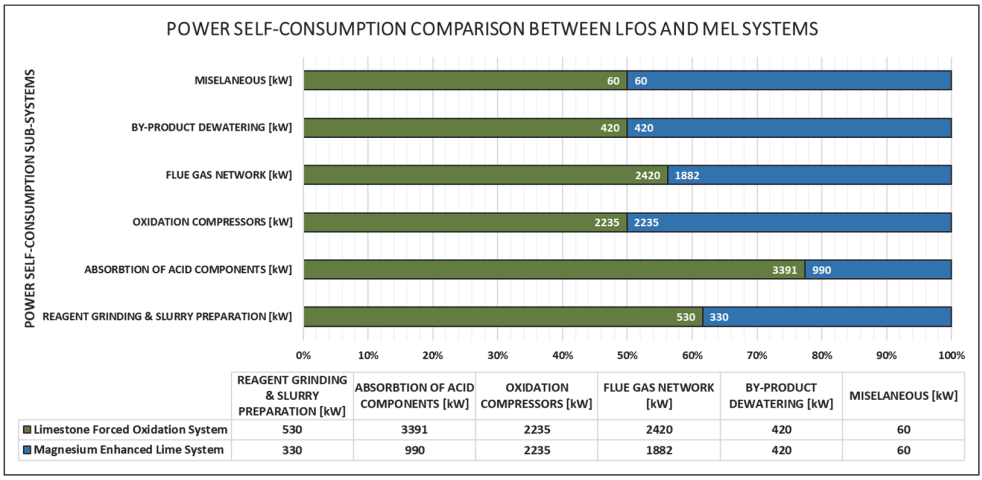

	REAGENT GRINDING & SLURRY PREPARATION [kW]	ABSORBTION OF ACID COMPONENTS [kW]	OXIDATION COMPRESSORS [kW]	FLUE GAS NETWORK [kW]	BY-PRODUCT DEWATERING [kW]	MISELANEOUS [kW]
Limestone Forced Oxidation System	530	3391	2235	2420	420	60
Magnesium Enhanced Lime System	330	990	2235	1882	420	60

Figure 5: *Power (electricity) self-consumption between limestone forced oxidation process and the magnesium-enhanced the lime process. The most significant savings at MEL process are available in the scope of the absorption of the acid components and the reagent grinding and slurry preparation.*

8 TECHNOLOGY APPLICATION CONSTRAINTS

There are some technical constraints of usage of the magnesium-enhanced lime desulphurization process applications. The absorber size of the magnesium-enhanced lime desulphurization process is limited due to engineering constraints and statical stability of the construction. In praxis, the individual units for the MEL desulphurization can range up to 1000 MW per boiler unit, for bituminous coals. The sulphur content in coal can range from 2% to 5% to still achieve the sufficient cleaning efficiency of the MEL process, which can up to 98% removal guarantees of SO_2 removal. The by-product of the MEL process can be disposed to the covered disposal area, although it can also be further used in the cement and construction industry. The main constraint of the usage of magnesium-enhanced lime desulphurization process is the availability of the reagent. Although there are some concerns that limestone contains a sufficiently high percentage of the magnesium in lime, it is very difficult to find a quarry of it in nature. As described previously, we can enhance the usual lime by adding magnesium to it, but this is not cost effective for the operation costs of the desulphurization process.

9 CONCLUSION

This paper has presented the alternative process of the wet calcite flue gas cleaning. The process presented uses magnesium-enhanced limestone as the reagent in the wet desulphurization process of flue gas cleaning. The disadvantages and advantages of such a process have been presented. The most favourable advantage of that process is its very reactive magnesium-enhanced limestone slurry, which eliminates the acid components in the flue gases. Because of the enhanced reactivity, the contact between the slurry and the flue gases can be shorter regarding the time needed for chemical reaction to fully recover acid components from the raw flue gases. That means smaller absorber unit, less spraying levels for the slurry, fewer recirculation pumps and a smaller amount of needed expensive construction materials to build the application. This directly results in smaller investment costs for such a desulphurization unit. The biggest disadvantage is the difficulty to find the needed reagent (limestone with the addition of the magnesium) in nature, i.e. at a quarry. If the reagent is not widely available in nature, such as limestone, this composition must be prepared and mixed with the proper mixture in a dedicated plant. That raises the operational costs of the magnesium-enhanced lime desulphurization process and makes it economically less-favourable for the installation in the existing thermal power plants. Nevertheless, the process is worth considering for the raw flue gases desulphurization process if the quarry of the proper reagent mixture is available in the surroundings of the existing thermo-electrical installation.

References

[1] **Sargent & Lundy**: *Wet Flue Gas Desulfurization Technology Evaluation*, Prepared for the National Lime Association, January 2003

[2] **A. Urankar:** *Izkušnje pri uporabi kotlovskega premoga v Termoelektrarni Trbolvje*, Strojniški Vestnik, Vol. 7-8, p.p. 129 - 134, Ljubljana 1978

[3] **R.K. Srivastava:** *Controlling SO_2 emissions: a review of technologies, National Risk Management Research Laboratory*, EPA/600/R-00/093, November 2000

[4] **J.B.Kitto, S.C. Stultz:** *Steam/its generation and use 41st edition*, The Babcock & Wilcox Company, Barberton, Ohio, U.S.A., 2005

[5] **J. Oman:** *Generatorji toplote*, Univerza v Ljubljani, Fakulteta za strojništvo, Ljubljana 2005

Nomenclature

(Symbols)	(Symbol meaning)
MEL	Magnesium Enhanced Lime
LFOS	Limestone Forced Oxidation System
pH	Level of acidity or alkalinity
Pa	Pascal
$Ca(OH)_2$	Calcium hydroxide
$Mg(OH)_2$	Magnesium hydroxide
$CaSO_3 \cdot ½H_2O$	Calcium sulphates
$MgSO_3$	Magnesium sulphide
$Mg(HSO_3)_2$	Magnesium disulphide
SO_2	Sulphur dioxide
$MgSO_4$	Magnesium sulfate
CaO	Calcium oxide

Journal of Energy Technology

JET Volume 11 (2018) p.p. 47-58
Issue 3, November 2018
Type of article 1.01
www.fe.um.si/en/jet.html

THEORETICAL ANALYSIS OF THREE PARAMETERS DETERMINING A THERMAL POWER CALIBRATION METHOD FOR THE TRIGA RESEARCH REACTOR

ANALITIČEN IZRAČUN TREH FAKTORJEV TERMIČNE KALIBRACIJE MOČI RAZISKOVALNEGA REAKTORJA TRIGA

doc. dr. Tomaž Žagar[1]

Keywords: research reactor, TRIGA, thermal power calibration

Abstract

Analytical analysis and calculation of factors relevant to the calorimetric power calibration method in the TRIGA research reactor are given. The calibration of nuclear instrumentation in the TRIGA research reactor is routinely done using a thermal power calibration method. The accuracy of the calorimetric thermal power calibration method depends on the accuracy of the thermal properties of the research reactor pool.

The most important properties of the reactor pool and the corresponding factors are reactor pool heat capacity, factor describing heat loss to the concrete wall, and the factor describing heat loss to the air above the pool. In this paper, these factors are first analytically calculated using only basic physical principles. The calculated values are compared to experimental values reported in the literature, and good alignment is observed.

This paper also has substantial educational value; it demonstrates that simple and basic analytical physics calculations can produce meaningful and useful results and can be validated against measured data obtained directly from experiments.

[1] GEN energija d.o.o., Vrbina 17, 8270 Krško, tomaz.zagar@gen-energija.si

Povzetek

Članek predstavlja analitičen izračun faktorjev, ki se redno uporabljajo pri termični kalibraciji jedrskih merilnikov raziskovalnega reaktorja TRIGA. V prispevku so obdelani naslednji trije faktorji, ki opisujejo termodinamične lastnosti raziskovalnega reaktorja TRIGA: toplotna kapaciteta reaktorskega bazena z vsemi elementi v njem, faktor toplotnih izgub s konvekcijo v zrak nad bazenom in faktor toplotnih izgub s prevajanjem skozi betonske stene reaktorskega bazena. Za vse tri faktorje je prikazan postopek izpeljave izračuna iz osnovnih fizikalnih enačb in principov brez uporabe numeričnih računskih metod. Analitično izračunane vrednosti so primerjane z eksperimentalno pridobljenimi rezultati. Ujemanje je v vseh primerih relativno dobro, še posebej pri izračunu integralnega podatka, kot je toplotna kapaciteta bazena. Članek ima tudi veliko pedagoško vrednost, saj prikaže kako lahko uporaba osnovnih fizikalnih principov in ustrezne poenostavitve pripeljejo do dobrih rezultatov.

1 INTRODUCTION

TRIGA[1] research reactors designed and supplied by General Atomics (*[1], [2]*) are an example of small and popular open-pool research reactors used for education and research in many countries. They are recognized as one of the most popular research reactor types worldwide, as more than 30 reactors have been built around the world and more than 10 reactors are still being regularly used. They are known for their inherent safety and versatility of use.

The purpose of this paper is to present and describe a reactor thermal power calibration method using the analytical approach from basic physical equations to final results, using only simple mathematical approaches and physical approximations without any numerical methods or more complicated mathematical models. The results of analytical calculations are then compared to recent experimentally determined and published results. The excellent experimental team at the TRIGA Mark II nuclear research reactor of the Jožef Stefan Institute (IJS) in Ljubljana recently performed several experiments. They measured temperature fields within the reactor pool for validation of different computational models and analysed the experimental results. The results were published in 2017 in several publications *[3]*, *[4]*, and *[5]*.

The second chapter in this paper gives a brief description of the TRIGA research reactor, limited to details needed for an understanding of the analysis. This chapter also contains a short background description of the thermal power calibration method, its purpose, and principles. The third chapter describes the calorimetric power calibration method with the analytical calculation of relevant constants and factors. In the final chapter, a comparison of calculated results and experimental results are presented.

[1] TRIGA: Test Research Isotope General Atomics, http://www.ga.com/triga

2 TRIGA RESEARCH REACTOR AND THERMAL POWER CALIBRATION

2.1 Short description of TRIGA research reactor and its systems

The analysis was performed for the 250 kW TRIGA Mark II reactor at IJS. A detailed description of the reactor with dimensions and other relevant data can be found elsewhere (the reader is directed, for example, to *[6]* or *[7]* and references contained therein). Only a brief description of the reactor needed for the understanding of this paper is presented here. The reactor is an open pool light water type. The core is annular and surrounded by a graphite reflector. It is at the bottom of a 6 m deep open aluminium tank with 2 m diameter containing approximately 20 m^3 of water. A general side view of the reactor with dimensions as built by General Atomics is presented in Figure 1 (a more detailed picture of the reactor can also be found in *[8]*).

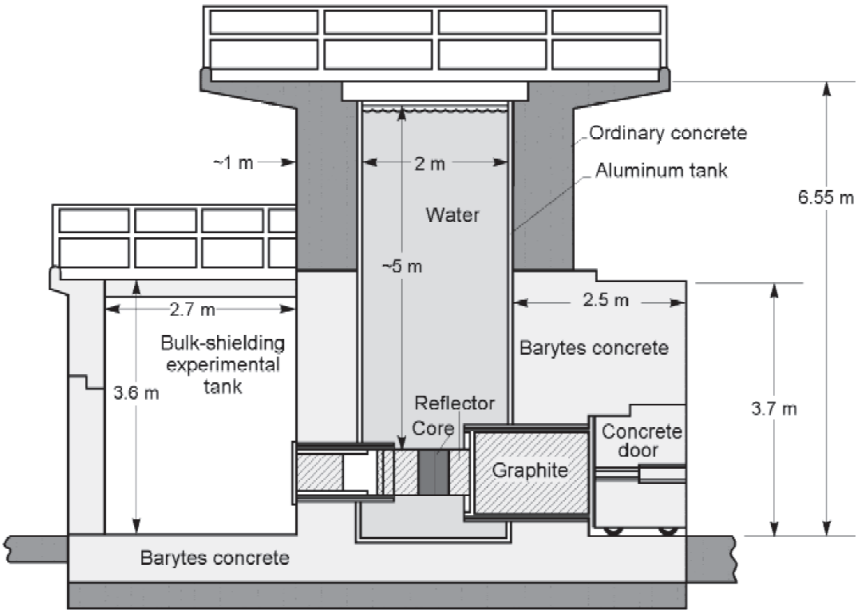

Figure 1: *Schematic side view of the TRIGA Mark II reactor at the Jožef Stefan Institute in Ljubljana, [7].*

The core is cooled by the natural convection and circulation of water within the tank. Heat generated in the reactor fuel is transferred to the water in the reactor core. Hot water rises from the core into the open tank water. Natural convection and circulation of the tank water are schematically presented in Figure 2. The pool water is later cooled using the closed secondary system presented in Figure 3. Water is circulated in a closed circuit through a heat exchanger in the basement of the reactor building.

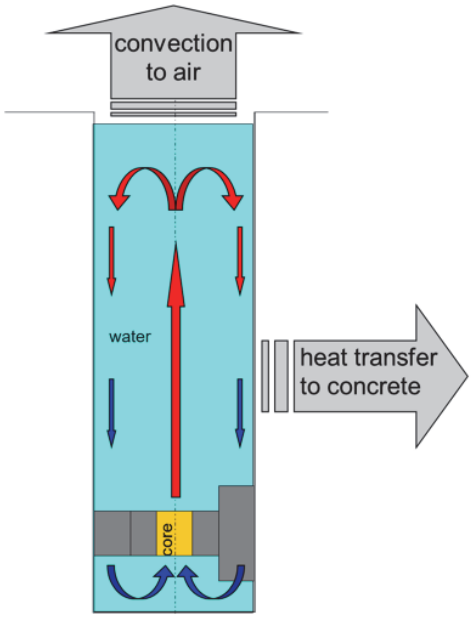

Figure 2: *Natural circulation of the water inside the reactor tank.*

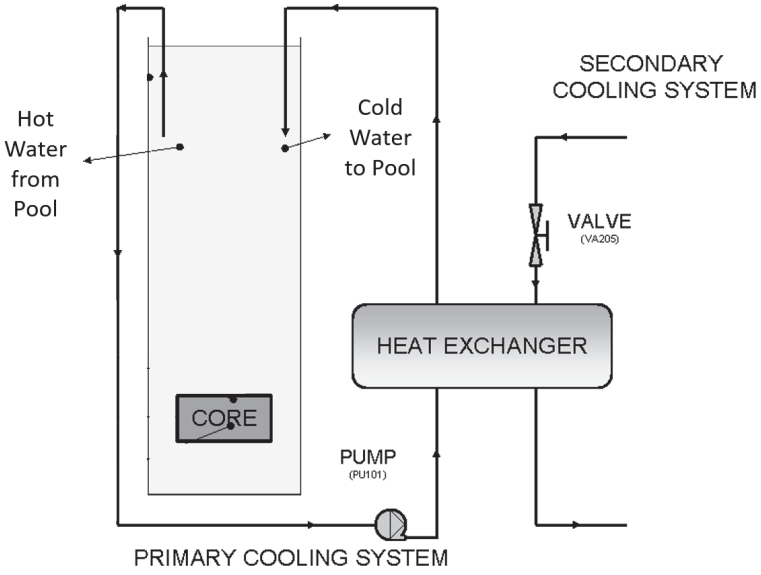

Figure 3: *Schematic diagram of TRIGA research reactor primary cooling system (natural circulation of the water inside the reactor tank).*

2.2 Reactor Thermal Power Calibration

Reactor thermal power is an important parameter for every reactor. Reactor thermal power Q is defined in terms of power released per fuel element, where P_j is a thermal power of each fuel element j. The power released per fuel element is the volumetric integral of the macroscopic fission cross section $\Sigma_f(E,r)$ and neutron flux $\phi(E,r)$ over each fuel element:

$$Q = \sum_{j=1}^{N} P_j = E_R \sum_{j=1}^{N} \int_0^E \int_{V_j} \Sigma_f(E,r) \times \phi(E,r) dE dV \quad , \qquad (1)$$

where N is the number of fuel elements in the core, and E_R is the normalization factor proportional to the fission energy released per each fission reaction, *[9]*.

A direct method to measure reactor power based on the definition given above would be to measure absolute thermal flux distribution across the core in all three dimensions. This is, of course, highly unpractical and usually almost impossible to do. Flux distributions could be measured with activation of cadmium-covered and bare foils irradiated by the steady reactor power. However, it should be realized that this method is extremely time consuming and not very accurate. This method is practical only for zero-power reactors and critical installations with no thermal generation. In reality, this method is very seldom performed for other research reactors and practically never for power reactors, *[9]*.

In the case of power reactors and research reactors in which a temperature rise across the core is produced and measured, a heat balance method is the most common and accurate method of determining the power output of the core.

In the heat balance method or the calorimetric method, the reactor thermal power is generally calculated from the measurements of the coolant temperature rise rates in the core or in the cooling system. For larger pressurized water reactors, the thermal power is calculated from the flow rate of the primary water and the temperature difference between water entering the reactor (cold leg) and hot water leaving the reactor (hot leg). In large reactors, coolant flow through the core is made by forced circulation driven by primary coolant pumps and is very well defined, controllable and can be measured accurately.

The heat balance method for the pool type reactors is slightly different since the flow through the core is driven by natural convection and is not so well constrained. Therefore, the thermal calibration method has to rely on the conventional calorimetric approach, based on temperature rise measurements of the entire pool structure.

The heat balance method based on a calorimetric method for the determination of the TRIGA research reactor power level proposed by the reactor's manufacturer (GA[2]) is performed according to the following procedure:

- Pool water, concrete, and air temperatures should be equal.
- Operate the reactor at constant power with primary cooling system switched off.
- Record the temperature rise of the pool water.

[2] GA stands for "General Atomic".

- Determine the temperature-rise rate ($\Delta T/\Delta t$).
- Calculate the reactor power as a function of the temperature-rise rate.

According to the procedure described above, reactor power Q depends only on the temperature-rise rate:

$$Q = K\frac{\Delta T}{\Delta t}, \tag{2}$$

where K is the reactor pool heat capacity constant. This is the first and most important factor, which will be calculated in the next chapter.

The first two points of the procedure above should guarantee that pool water is well insulated from the environment and that there are no heat losses to concrete or reactor building ambient air. In reality, this is seldom the case, so we will also calculate two factors for correcting these losses.

3 CALCULATION OF POOL HEAT CAPACITY AND HEAT LOSS CONSTANTS

3.1 Reactor Pool Heat Capacity Constant Calculation

Reactor pool heat capacity constant K can be calculated rather quickly if we assume that the reactor pool temperature is constant throughout the pool and neglect all heat loss from the pool. In other words, we can approximate the reactor pool as an insulated "point pool" model. We can treat the reactor pool as well insulated when the water temperature is equal to air and concrete temperatures. Thus, the reactor heat capacity K can be simply calculated from wet pool volume V_w:

$$K = \rho \times \mathrm{V_w} \times c_p, \tag{3}$$

where ρ is water density and c_p is water specific density. Heat capacity constant calculated using equation (3) are presented in Table 1 below for two very similar reactors (TRIGA research reactor at the Jožef Stefan Institute and the TRIGA research reactor at the University of Vienna). The results for the TRIGA research reactor in Ljubljana are from recent experiments, while the results for a research reactor in Vienna are from experiments reported some years ago, *[10]*. Note that all thermophysical properties of water in this calculation were evaluated for 20°C.

Table 1: *Calculated and measured reactor heat capacity constants*

	V_w [m³]	K calculated in this paper [kWh/K]	K measured (as reported) [kWh/K]	K given as a reference by manufacturer (GA) [kWh/K]
Ljubljana	17.6	20.4	19.6 ± 0.3 [3]	19.05
Wien	16.5	19.1	19.2 ± 0.3 [10]	18.48

The point pool model used for this approximation is valid only if very good mixing is present in the pool. To analyse the speed and rates of pool water mixing, we used the TRISTAN software, *[11]*, which is designed for the steady-state thermal-hydraulic analysis of TRIGA research reactors cooled by natural convection, operating at a low power level (below 1 MW) in open pools. The software calculates the speed of water flowing through the cooling channels in the core of the reactor for different conditions of the research reactor. The calculated flow parameters and average coolant speed in the cooling channel are presented in Figure 4, in which the average speed of water in the coolant channel against the reactor power is presented. These results calculated using TRISTAN compare very well with a more detailed thermal hydraulics computational model of the reactor tank and calculations performed recently, in which the average calculated water velocity at full reactor power in the cooling channels was in the range from 0.09 to 0.12 m/s, *[5]*. This compares well with a velocity of 97 cm/s, presented in Figure 4, calculated at full reactor power (250 kW).

The results show that the water speed in the reactor core is increasing with increasing reactor power. However higher speed does not also produce better mixing. In the pool, mixing is presented as a number of total wet pool volume V_w circulations through the reactor core before the average temperature in the pool increases by 4°C. The rate of pool water circulation through the reactor core was calculated on the basis of the average water speed in the coolant channel and coolant channel cross section. This number is presented in Figure 4 as the number of the entire pool volume circulation through the reactor core in the time of one calorimetric calibration procedure. The time for one calibration is taken to be equal to the time in which the bulk water temperature in the pool increases by 4 °C. As can be seen from this picture, the point pool approximation can be acceptable only for very low calibration powers. For higher powers, the temperature in the reactor pool increases too fast, and the pool is not at a homogeneous temperature. For example, at approximately 140 kW, only half of the pool volume circulates through the core before the calibration procedure is complete. The homogeneous point pool model can be accepted as a good approximation only for low powers (e.g. 20 kW or less) when the water circulation rate is big enough to promote good mixing in the pool. With higher reactor powers the water circulation rate is becoming smaller, and the fluctuations are becoming bigger.

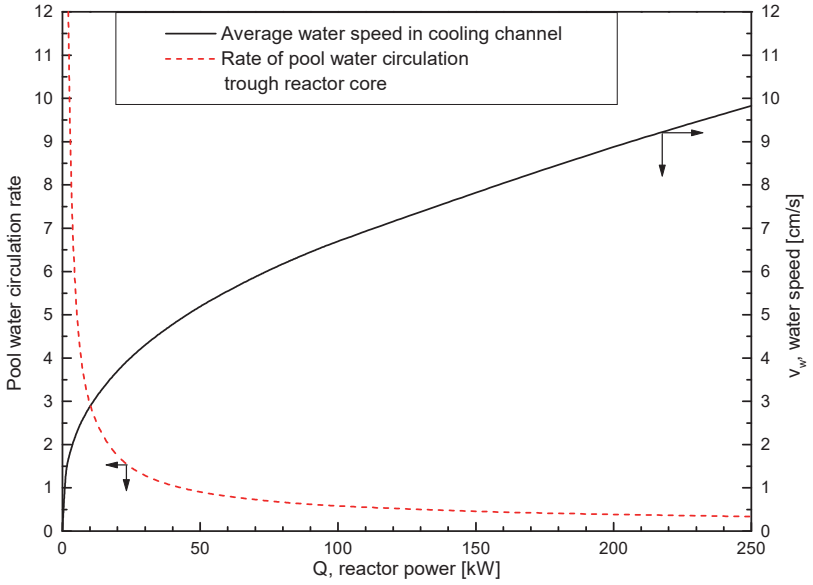

Figure 4: *Calculated average water speed in cooling channel and the pool water circulation rate through reactor core as a function of reactor thermal power.*

3.2 Calculation of Heat Loss by Convection to Reactor Ambient Air

In many cases, thermal power calibration is not performed under ideal conditions. During winter, concrete and air temperatures are lower than water temperature, and in summer they are sometimes higher. In these cases, the reactor pool also loses heat to concrete walls and ambient air, and thermal convection and conduction must be considered to estimate heat loss from the reactor pool accurately.

When the air temperature T_{air} is higher than bulk pool temperature T_{water} , thermal conditions above the reactor pool are stable, and there is no convection. In this case, the heat transfer from air to water occurs only by convection through the air, which can be neglected. However, in the opposite case, the heat transfer occurs from the pool to the open air by natural convection. The rate of heat convection from pool surface to the air can be estimated according to Newton's law of cooling, *[12]*:

$$q'' = h \times \left(T_{air} - T_{water}\right). \tag{4}$$

The average convection heat transfer coefficient *h* can be expressed in terms of the Nusselt number:

$$Nu_L = \frac{hL}{k}, \tag{5}$$

where *k* is the thermal conductivity of air, and *L* is the characteristic length of the pool surface, which is:

$$L \equiv \frac{A}{D}. \tag{6}$$

A is the surface area, and *D* is the surface perimeter. The Nusselt number for the horizontal surface is, *[12]*:

$$Nu_L = 0.15 Ra_L^{1/3} \text{ for } (10^7 < Ra_L < 10^{11}). \tag{7}$$

The Rayleigh number is a product of the Grashof number and the Prandtl number and can be expressed as:

$$Ra_L = \frac{g \times \beta \times (T_{air} - T_{water}) \times L^3}{\alpha \times \nu}, \tag{8}$$

where *g* is gravitational acceleration, *β* is air volumetric thermal expansion coefficient, *ν* is air kinematic viscosity (also called "momentum diffusivity"), and *α* is air thermal diffusivity.

With these equations and with the thermophysical properties of air evaluated for 20°C, we obtain the following results:

$$Ra_L = 3.4 \times 10^8 \times \Delta T \frac{1}{K} \text{ and } h = 1.8 \times \Delta T^{1/3} \frac{W}{m^2 K^{4/3}};\ \Delta T = T_{air} - T_{water}. \tag{9}$$

Total heat loss to air is then:

$$Q_{loss}^{air} = A \times q'', \tag{10}$$

$$Q_{loss}^{air} = 13.6 \times (T_{air} - T_{water})^{4/3} \frac{W}{K^{4/3}}. \tag{11}$$

3.3 Calculation of Heat Loss by Conduction to Pool Concrete

When concrete temperature $T_{concrete}$ is different from the bulk water temperature, some heat transfer from or to the concrete occurs. The heat transfer can be estimated with heat conduction through concrete:

$$q'' = \frac{k}{d} \times (T_s - T_{concrete}), \tag{12}$$

where *k* is concrete thermal conductivity, *d* is the distance between the pool wall and concrete temperature measuring position and T_s is pool wall temperature. Furthermore, with heat convection from the pool wall to pool water:

$$q'' = h \times (T_{water} - T_s), \tag{13}$$

where *h* is the average natural convection heat transfer coefficient, which can be expressed in terms of the Nusselt number given in equation (5). The Nusselt number for free convection on a vertical surface in the turbulent region is:

$$Nu_H = 0.10 \times Ra_H^{1/3}. \tag{14}$$

For vertical plates, the critical Rayleigh number is 10^9. In our case, for water at 20 °C, the Rayleigh number is:

$$\mathrm{Ra_H} = 16 \times 10^9 \times \Delta T \times H^3 \frac{1}{m^3 K};\ \Delta T = T_{water} - T_s, \tag{15}$$

where H is the vertical position on the pool wall. As can be seen from the result above, the natural convection boundary layer is even for very small temperature differences in the turbulent region, and equation (14) is justified.

From equations (12), (13) and (10), we obtain the final result for heat loss:

$$Q_{loss}^{concrete} = \frac{37.99 \times \Delta T}{(0.143 + 0.007 \times \Delta T^{-1/3} K^{1/3})} \frac{W}{K};\ \Delta T = T_{concrete} - T_{water}. \tag{16}$$

For small temperature differences, this equation can be reasonably well approximated with the equation:

$$Q_{loss}^{concrete} = 250 \times (T_{concrete} - T_{water}) \frac{W}{K}. \tag{17}$$

4 COMPARISON BETWEEN CALCULATED AND MEASURED RESULTS

The analysis presented in the previous chapter was simple, but as we will see in this chapter, it gives good results in comparison to measured values. Certainly, the calculations are easier to perform than experimental measurements. Reliable experimental results can only be obtained with well-defined and controlled experiments. Fortunately, a well-planned and well-prepared experimental campaign was performed recently at the TRIGA research reactor at the Jožef Stefan Institute, and the results were reported in a paper by Štancar and Snoj in 2017, *[3].*

During the experimental campaign performed by Štancar and Snoj, exact measurements of several parameters were performed. Among the measured parameters, there were also three parameters calculated in the previous chapter: heat capacity constant, values of convective heat transfer to air, and values of conductive heat transfer to concrete. With this information, we can make a direct comparison between calculated and experimental values, and this comparison is presented in Table 2.

Experimental heat capacity constant results were presented in Table 1. The heat capacity constant was calculated using equation (3) in this paper. Experimental values for convective heat losses to air are taken from Table 3 in *[3]*. Convective heat losses to ambient air in reactor hall were calculated with equation (11) in this paper. Experimental values for conductive heat transfer to concrete are taken from Table 4 in *[3]*. Conductive heat losses from the pool water to the concrete in the pool walls were calculated with equation (17) in this paper.

Table 2: *Comparison of the calculated and measured values*

Parameter	Calculated values	Calculated values	Measured values	Measurement reference	C/E
Heat Capacity Constant equation (3)	V_w [m³]	*K* [kWh/K]	*K* [kWh/K]		
	17.6	20.4	19.6 ± 0.3	[3]	1.04
	16.5	19.1	19.2 ± 0.3	[10]	0.99
Heat Convection to Reactor Hall Air equation (11)	T_{water} - T_{air} [K]	Q^{air} [W]	Q^{air} [W]		
	3.8	81	33	[3]	2.45
	7.5	200	76	[3]	2.63
Heat Conduction to Reactor Concrete Wall equation (17)	T_{water} - T_{conc} [K]	Q^{conc} [W]	Q^{conc} [W]		
	3.2	800	1100 ± 100	[3]	0.73
	6.2	1550	2100 ± 300	[3]	0.74

Although the methods used were rudimental and we used a significant amount of approximation, the results are relatively good, since all results are in general agreement. The results are very good for an integral parameter (Heat Capacity Constant), for which the discrepancy between calculation and experiment is less than 5%. Even for more complex and smaller effects (on the scale of few watts and up to a kilowatt), the rudimentary approach gives reasonably good results.

5 CONCLUSIONS

The analytical approach presented in this paper can be used to better understand the physical processes during the calorimetric power calibration in the TRIGA research reactor. To measure correct temperature-rise rates, the measurement should be performed at low reactor power, with concrete and air temperatures equal to the bulk water temperature. Under controlled conditions, corrections for heat losses are small and do not exceed more than 2 kW (this is less than 1% of the reactor power, which is 250 kW). Even for such small corrections, the analytical approach presented in the paper presents reasonable results, demonstrating our correct understanding of the basic physical processes taking place in the reactor pool and its surroundings during the reactor core heat up.

Based on the results of this analytical approach, we can also conclude that calorimetric power calibration can be significantly wrong if it is performed under uncontrolled conditions. If the calorimetric calibration is performed with high reactor power or with water temperature lower than concrete temperature, the error can be as big as 30%.

References

[1] **M. T. Simnad et al.**: *Nuclear Technology 28*, 31, 1976

[2] **M. T. Simnad:** Nuclear Engineering and Design 64, 403, 1981

[3] **Ž. Štancar and L. Snoj:** Nuclear Engineering and Design 325, 78, 2017

[4] **R. Henry, I. Tiselj and M. Matkovič:** Heat and Mass Transfer 53, 2, 537-551, 2017

[5] **R. Henry, I. Tiselj and L. Snoj:** Annals of Nuclear Energy 110**,** 36–47, 2017

[6] **T. Žagar et al:** Journal of Nuclear Materials 335, 379, 2004

[7] **T. Žagar and M. Ravnik:** Nuclear Technology 140, 113, 2002

[8] **M. Ravnik and R. Jeraj:** Nuclear Science Eng. 145, 145–152, 2003

[9] **J. Shaw:** "Reactor Operation", Pergamon Press, Oxford, 1969

[10] **A. Breymesser et al:** "Thermal power calibration of the TRIGA reactor Wien", 2nd Regional Meeting: Nuclear Energy in Central Europe, (Proc. Reg. Meet. Portorož, 1995), Nuclear Society of Slovenia, Ljubljana, Slovenia, 1995

[11] **I. Mele and B. Žefran:** "TRISTAN - A Computer Program for Calculating Natural Convection Flow Parameters in TRIGA Core", IAEA1337, OECD NEA Data Bank, IJS-DP-6548, Institute "Jožef Stefan" Report, 1992

[12] **F.P. Incropera and D.P. DeWitt:** "Fundamentals of Heat and Mass Transfer", John Wiley & Sons, New York, 1996

Journal of Energy Technology

JET Volume 11 (2018) p.p. 59-69
Issue 3, November 2018
Type of article 1.04
www.fe.um.si/en/jet.html

THE EFFICIENCY OF MAGNETIC REFRIGERATION AND A COMPARISON WITH COMPRESSOR REFRIGERATION SYSTEMS

UČINKOVITOST MAGNETNEGA HLAJENJA IN PRIMERJAVA S KOMPRESORSKIM HLADILNIM SISTEMOM

Botoc Dorin[✉1,1,2], Jurij Avsec[1], Adrian Plesca[2]

Keywords: Magnetocaloric effect, magnetic refrigeration, compressor refrigeration, heat transfer.

Abstract

The objective of this paper is to study the magnetic refrigeration process that makes use of solid materials, such as gadolinium silicon compounds, as the refrigerant. This effect was observed many years ago and was used for cooling to low temperatures. Recently, materials are being developed with which sufficient temperature and entropy change are produced which makes them useful for a wide range of refrigeration applications. Magnetic refrigeration is an emerging technology that utilizes this magnetocaloric effect found in a solid state to produce a refrigeration effect.

✉1 Corresponding author: Botoc Dorin, E-mail address: dorinbotoc@yahoo.com

[1] University of Maribor, Faculty of Energy Technology, Laboratory for Thermomechanics, Applied Thermal Energy Technologies and Nanotechnologies, Hočevarjev trg 1, SI-8270 Krško, Slovenia

[2] Faculty of Electrical Engineering, Energetics and Applied Informatics, Gheorghe Asachi Technical University of Iasi, Department of Power Engineering, Romania

Povzetek

Namen prispevka je preučiti magnetno hlajenje, v katerem se kot hladilno sredstvo uporabljajo trdni materiali, kot so na primer goldolinijeve silicijeve spojine. Ta učinek je bil opazen pred mnogimi leti in je bil uporabljen za hlajenje blizu absolutne ničle temperature. V zadnjem času se razvijajo materiali, v katerih se proizvaja zadostna temperaturna razlika in sprememba entropije, zaradi česar so uporabne za uporabo v širokem razponu temperature. Magnetno hlajenje je nastajajoča tehnologija, ki uporablja ta magnetno-kalorični učinek v trdnem stanju, da proizvede hladilni učinek.

1 INTRODUCTION

Modern society mostly uses vapour compression cycles and vapour absorption cycle processes. Moreover, using refrigerants such as chlorofluorocarbons or hydrochlorofluorocarbons (CFCs and HCFCs) have adverse effects on our environment. Recently, the developments of new technologies such as magnetic refrigeration and thermoelectric refrigeration, have brought alternatives to the conventional gas compression technique. One of the most important researchers in this field was Prof. Emil Gabriel Warburg (1846-1931) *[1]*, a German physicist and a professor of physics at the Universities of Strasbourg, Freiburg and Berlin. In 1881, he discovered the magnetocaloric effect in an iron sample. Magnetic refrigeration is a cooling technology based on this effect. This method can be used to attain low temperatures, as well as the ranges used in common refrigerators, depending on the design of the system.

2 WORKING PRINCIPLE OF MAGNETIC REFRIGERATION SYSTEM

Magnetic refrigeration works on the principle of the magnetocaloric effect (MCE), which is a magneto-thermodynamic phenomenon in which a reversible change in temperature of a suitable material is caused by exposing the material to a changing magnetic field, *[1-8].*

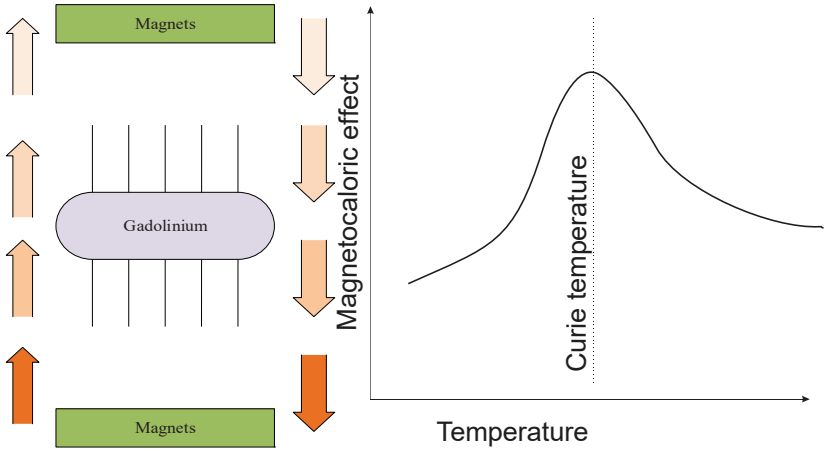

Figure 1: *Magneto-caloric effect*

MCE is the behaviour of a magnetic solid when it is exposed to a changing magnetic field: its temperature may be appreciably increased or decreased, with both the sign and the extent of the temperature difference between the final and the initial states of the material being dependent on numerous intrinsic and extrinsic factors. The chemical composition, the crystal structure, and the magnetic state of a compound are among the most important material parameters that determine its MCE. Magnetic refrigeration is based on a fundamental thermodynamic property of magnetic materials: the so-called magnetic effect, which causes a temperature change if the material is subject to an applied magnetic field under adiabatic conditions.

3 THERMODYNAMICS OF THE MAGNETIC REFRIGERATION SYSTEM

The basic thermodynamic cycle of the magnetic refrigerator is the Ericsson cycle, which operates between two adiabatic and two isomagnetic field lines. The magnetic refrigeration system can be divided into four fundamental steps (Fig. 2, Fig. 3). The temperature of hot and cold heat exchangers has agreat influence on the refrigeration performance, *[1-8].*

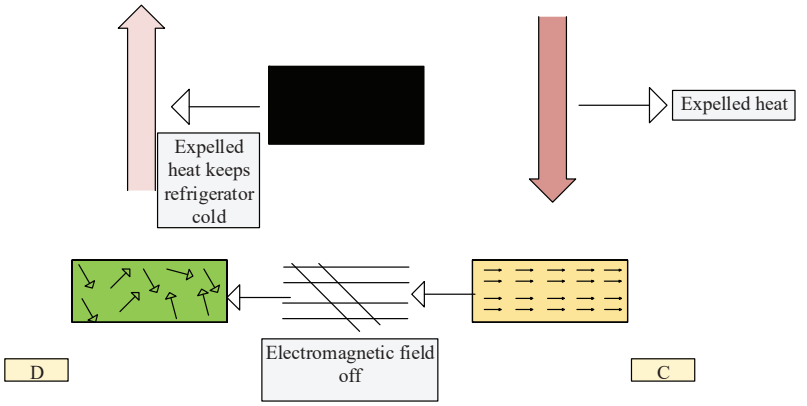

***Figure 2**: Thermodynamic processes in magnetic refrigeration*

1. Adiabatic magnetization: A magnetocaloric material, when placed in an insulated environment(Q=0) and the external magnetic field is increased (+H), causes the magnetic dipoles of the atoms to align, thereby decreasing the material's magnetic entropy and heat capacity.
2. Isomagnetic enthalpy transfer: The magnetic field is held constant during this process (H=0) and the heat added during the adiabatic magnetization is then removed (-Q) by a fluid or gaseous substance to prevent the dipoles from reabsorbing the heat.

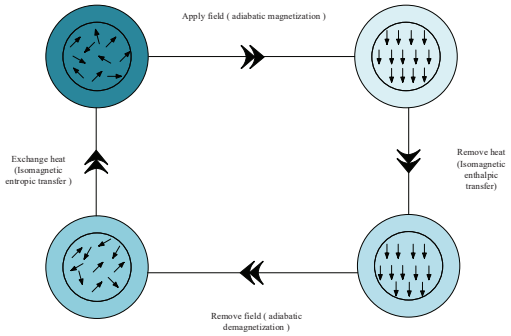

***Figure 3:** Thermodynamic processes in magnetic refrigeration*

3. Adiabatic demagnetization: The substance is returned to another adiabatic process (Q=0), and hence the total entropy remains constant. However, this time the magnetic field is reduced, the thermal energy causes the magnetic moments to overcome the field, and thus the sample cools, i.e. an adiabatic temperature change.
4. Isomagnetic entropic transfer: The magnetic field is held constant to prevent the material from heating back up.

The magnetic field sources that can be used in magnetocaloric devices are permanent magnets and electromagnets. From the theory, we could divide magnetic refrigeration systems into refrigeration systems with moving parts (rotary, linear) or without moving parts. This machine uses as magnetocaloric suspensions working fluid.

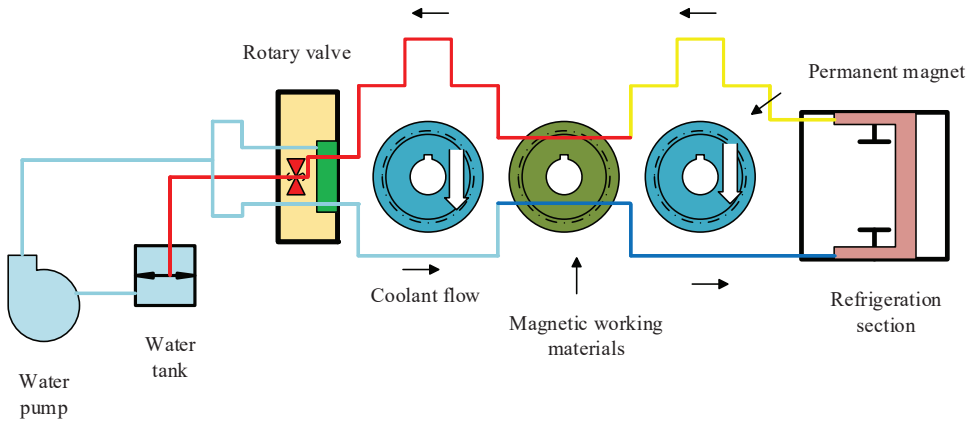

Figure 4: *Components of a magnetic refrigeration system*

Fig. 4 presents a rotational magnetic refrigeration system. Heat is exchanged by means of a circulating coolant (water). Because the magnets rotate, the magnetic working material is repeatedly heated and cooled. The well-timed switching of the direction of coolant flow in coordination with the rotation of the magnets enables cooled coolant to be supplied to areas to be cooled, *[17].*

Generally speaking, a compressor refrigeration system comprises two exchangers, with one receiving heat from the environment (evaporator) and the other releasing heat to the heating water (condenser) by means of a compressor, an expansion valve, and connecting copper pipes (Figure 5). Naturally, a refrigerant is required for the operation of a compressor refrigeration system. Refrigerants are working fluids, transferring heat from a lower temperature level to a higher temperature level. Decades ago, chlorofluorohydrocarbons were widely used for refrigerants in cooling and heating systems. As a result of stricter environmental laws and measures and claims that these refrigerants damage the ozone layer, their application started to be phased out. The use of new pure refrigerants and mixtures of more environmentally friendly and degradable refrigerants has been increasingly adopted, in case they are unexpectedly released into the environment.

The coefficient of performance (COP) of a magnetic refrigerator is the measurement of the thermodynamic quality of the apparatus under consideration; it shows how much (electrical) power P is to be invested for cooling Q_r, [16]

$$COP = \frac{\dot{Q}_r}{P} \tag{3.1}$$

$$\dot{Q}_r = \begin{Bmatrix} \dot{Q}_L - \Delta\dot{Q}, \Delta\dot{Q} > 0 \\ \dot{Q}_{L,} \Delta\dot{Q} < 0 \end{Bmatrix} \tag{3.2}$$

$$\Delta\dot{Q} \quad = \dot{Q_{bc}} - \dot{Q_{da}} \tag{3.3}$$

In refrigeration units applying superconducting magnets, the efficiency would be further reduced due to the power demand of the magnetic field sources as well as of the supporting cryogen system.

In this way, the compressor coefficient of performance (COP) in the cooling mode may be defined (Figure 5):

$$COP = \frac{\dot{Q}_{evap}}{P} = \frac{\dot{m}(h_1 - h_4)}{P} \tag{3.4}$$

4 COMPARISON BETWEEN MAGNETIC AND COMPRESSOR REFRIGERATION SYSTEMS

In this chapter, we will analyse magnetic and compressor refrigeration systems for a family house with the required cooling heat of 11 kW. As the refrigerant, we have used refrigerant R-134a in an ideal compression refrigeration cycle. For the modelling of the compressor refrigeration process, we have used the following boundary conditions:

- temperature in the condenser 40^0C
- temperature in the evaporator -7^0C.

The presented analysis is used for the 11 kW required refrigeration heat for summer house cooling.

$$h_1 = 574, h_{2s} = 600\,\frac{kJ}{kg}, h_3 = h_4 = 480\,\frac{kJ}{kg} \tag{4.1}$$

With the isentropic efficiency of the compressor of 85% we obtain the enthalpy h_2:

$$h_2 = h_1 + \frac{1}{\eta_s}(h_2 - h_1) = 574 + \frac{1}{0.8}(600 - 574) = 606\ kJ/kg \tag{4.2}$$

The performance of refrigerators and heat pumps is expressed in terms of the coefficient of performance (COP) defined as:

$$COP_R = \frac{Desired\ output}{Required\ input} = \frac{Cooling\ effect}{Work\ input} = \left|\frac{h_1 - h_4}{h_1 - h_2}\right| = \left|\frac{574-480}{574-606}\right| = 2.94 \tag{4.3}$$

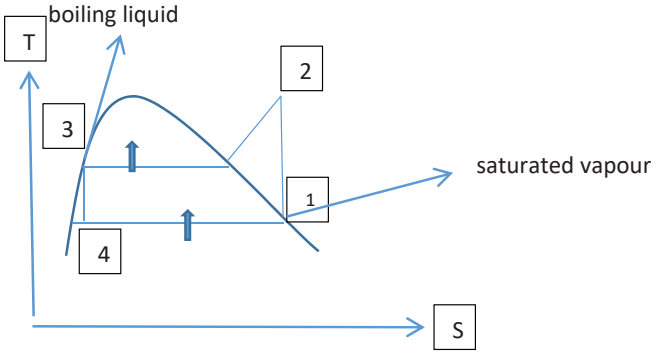

Figure 5: *Ideal compressor refrigeration cycle*

Table 1: *Processes in compressor refrigeration cycle*

Process	Description
1-2	Isentropic compression
2-3	Constant pressure heat rejection in the condenser
3-4	Throttling in an expansion valve
4-1	Constant pressure heat rejection in the evaporator

Compressor power can be calculated from the relation:

$$P_{comp} = \frac{Q_{evap}}{COP} = \frac{11}{2.94} = 3.74\ kW$$

(4.4)

The energy consumed by the compressor per day

$$W_{day} = 3.74 \cdot 24 = 89.67\ kW\ per\ day$$

(4.5)

The energy consumed by the compressor per month

$$W_{month} = 89.67\ \cdot 31 = 2782\ kWh\ per\ month$$

(4.6)

The cost of energy per month

$$C = 2782 \cdot 0.13 = €361.6 \qquad (4.7)$$

Cost per kWh –€0.13 (4.8)

The magnetic refrigeration system

The most important characteristic's of a magnetocaloric device is its efficiency. It is usually defined by the Coefficient Of Performance (COP). The COP presents a ratio between the refrigeration energy and the total electric energy input. According to the literature [9] the required electric power could be determined this way:

$$P_{el} = \frac{Q_r}{COP} = \frac{11}{9.09} = 1.21\ kW$$
(4.9)

Where:

P_{el} – the energy consumed by the electric motor

The energy consumed by the motor per month

$$W_{month} = 1.21 \cdot 24 \cdot 31 = 900.2 \quad (4.10)$$

The cost of energy per month

$$C = 900.2 \cdot 0.13 = 117.0€ \quad (4.11)$$

***Table 2**: Compression Efficiency between classical heat pump and with magnetic heat pump*

Efficiency for heat pump	Efficiency for magnetic heat pump
2.94	9.09
Consumed energy for compressor	Consumed energy for compressor
2782 kWh/month	900.2 kWh/month
The cost of energy/month	The cost of energy/month
€361.6	€117

***Table 3:** Economic analyses for, cost of installation, energy, maintenance and equipment for classical heat pump and magnetic heat pump [16]*

Initial cost		Compressor refrigeration system	Magnetic refrigeration system		
Cost of equipment	€	10000	25000	Difference	15000
Cost of installation	€	3000	1500	Difference	1500
Total initial cost	€	13000	26500	Difference	13500

Annual operating cost		Heat pump	Magnetic heat pump		
Energy consumption	kWh	25176	9816	Difference	15360
Cost of energy	€	3276	1276	Difference	2000
Cost of maintenance	€	1800	1200	Difference	600
Total annual cost	€	5073	2476	Difference	2597

From the analysis of Tables 2 and 3, it can be seen that the purchase of the magnetic cooling system is still significantly more expensive, while the cost of the heating is considerably lower, especially due to a better cooling number. The purchase of the magnetic cooling system pays for itself after around six years. Some benefits and disadvantages of the magnetic refrigeration system are as follows, *[16].*

Benefits:

1. Environmentally friendly - Refrigerant used is solid and non-volatile and hence has no greenhouse effect. Conventional refrigerators use refrigerants that contain CFC or HCFC, which have been linked to ozone depletion and global warming. Some refrigerants, such as ammonia, are toxic and flammable.
2. Low running and operating cost - There is no compressor, which is the most inefficient and costly part, in magnetic refrigerators. This leads to less energy consumption and hence low running costs.
3. Higher efficiency - Because it eliminates the need to expand and compress the liquid, a magnetic refrigerator consumes less energy and can operate at 60% efficiency.
4. Reliability - High energy density and more compact device, fewer moving parts in comparison to traditional systems and thus more reliable.
5. Quiet operation - This refrigerator unit is substantially quieter than traditional refrigeration systems.
6. Compactness: - It is possible to achieve a high energy density compact device. This is because in case of magnetic refrigeration the working substance is a solid material (e.g. gadolinium) and not a gas as in the case of vapour compression cycles

Disadvantages:

1. The initial investment is very high in comparison to conventional refrigeration.
2. The magnetocaloric materials are rare earth materials hence their availability also becomes a disadvantage. These materials need to be developed to allow larger frequencies of rectilinear and rotary magnetic refrigerators.
3. Protection of electronic components from magnetic fields. However, it must be noted that they are static, of short range and may be shielded
4. Permanent magnets have limited field strength, while electromagnets and superconducting magnets are very expensive.
5. Temperature changes are limited. Multi-stage machines lose efficiency through the heat transfer between the stages.
6. Moving machines need high precision to avoid magnetic field reduction due to gaps between the magnets and the magnetocaloric material.

5 CONCLUSION

This article presents thermodynamic and economic analysis between magnetic refrigeration system and a conventional refrigeration system. From the analysis, it can be seen that the purchase of the magnetic cooling system is still significantly more expensive, while the cost of heating is considerably lower. The return period for the purchase of the magnetic cooling system is approximately six years.

References

[1] **Y. Kulkarni:** *A review on Magnetic Refrigeration at Room Temperature*, International of Innovative Research in Science, Engineering and Technology, Vol. 4, Iss. 12, 2015

[2] **Q. Mary:** *Novel Thermodynamic Cycles involving Ferrofluids displaying Temporary Magnetic Remanence*, School of Engineering and Material Science, p.p.69-73, 2013

[3] **E. Gedic, M. Kaufeci, A. Kecebas, H. Kurt:** *Magnetic refrigeration technology applications on near-room temperature*, International Advanced Technologies Symposium Karabuk Turkey, 2009

[4] **U. Lucia:** *Exergy analysis of magnetic refrigeration*, Spalto Marengo Alessandria, 2010

[5] **P. W. Egolf, A. Kitanovski, D. Vuarnoz, M. Diebold, C. Besson**: *An Introduction to magnetic refrigeration*, Institute of Thermal Sciences, Switzerland CH 1401

[6] **Dr. Terry, J.Hendricks, Valerie H.Johnson, Matthew A.Keyser:** *Heat- Generated Cooling Opportunities*, Center for Transportation Technologies and System, Colorado

[7] **V. K. Pecharsky, K. A.Gscheidner:** *Magnetocaloric Materials*, Iowa State University, USA

[8] **A. Kitanovski, V. Plaznic, J. Tusek, A. Poredoš:** *New thermodynamic cycles for magnetic refrigeration*, International Journal of refrigeration 37, ELSEVIER, 2014

[9] **N. Biswas, N. K.Hanna, P. Datta, P.S. Mahapatra:** *Analisys of heat transfer*, Journal Power Technology, ELSEVIER, 2018

[10] **S. Labrosse:** *Thermal evolution of the core with a high thermal conductivity*, Journal of Physics of the Earth and Planetary Interiors, 2012

[11] **J. Tusek, S. Zupan, I. Prebil, A. Poredos:** *Magnetic Cooling-Development of Magnetic Refrigeration*, Journal of Mechanical Engineering, Slovenia, 2009

[12] **Z.G.Zheng, Y.Yu, X.C.Zhong, D.C.Zeng, Z.W.Liu:** *Design and performance study of the active magnetic refrigerator for room-temperature application*, International Journal of refrigeration 32, 2009

[13] **A. Rowe, A. Tura, J. Dikeos and R. Chahineb:** *Near Room Temperature Magnetic Refrigeration*, Proceedings of the International Green Energy Conference, Waterloo, Ontario, Canada, 2005

[14] **J. Avsec, U. Novosel:** *Control of air conditioning*, 1st ed. Maribor: University of Maribor Press, 2017

[15] **M. Arnemann:** *Energy efficiency of Refrigeration System*,Karlsruhe UAS Institute of Refrigeration, Air Conditioning and Environmental Enginering (IKKU) 76133, Karlsrache Germany

[16] **Bjørk, Rasmus; Smith, Anders; Bahl, Christian; Pryds, Nini:** *Determining the minimum mass and cost of a magnetic refrigerator,* Technical Universy of Denmark 2011

[17] System developed by Railway Institute for evaluation of performance of magnetic working materials

Nomenclature

t	time
v	specific volume
COP	coefficient of performance
Q	heat released

Journal of Energy Technology

Author instructions

www.fe.um.si/en/jet.html

MAIN TITLE OF THE PAPER
SLOVENIAN TITLE

*Author[1], Author [2], Corresponding author*ℜ

Keywords: (Up to 10 keywords)

Abstract

Abstract should be up to 500 words long, with no pictures, photos, equations, tables, only text.

Povzetek

(Abstract in Slovenian language)

Submission of Manuscripts: All manuscripts must be submitted in English by e-mail to the editorial office at jet@um.si to ensure fast processing. Instructions for authors are also available online at http://www.fe.um.si/en/jet/author-instructions.html.

Preparation of manuscripts: Manuscripts must be typed in English in prescribed journal form (MS Word editor). A MS Word template is available at the Journal Home page.

A title page consists of the main title in the English and Slovenian language; the author(s) name(s) as well as the address, affiliation, E-mail address, telephone and fax numbers of author(s). Corresponding author must be indicated.

Main title: should be centred and written with capital letters (ARIAL bold 18 pt), in first paragraph in English language, in second paragraph in Slovenian language.

Key words: A list of 3 up to 6 key words is essential for indexing purposes. (CALIBRI 10pt)

Abstract: Abstract should be up to 500 words long, with no pictures, photos, equations, tables, - text only.

Povzetek: - Abstract in Slovenian language.

Main text should be structured logically in chapters, sections and sub-sections. Type of letters is Calibri, 10pt, full justified.

ℜ Corresponding author: Title, Name and Surname, Organisation, Department, Address, Tel.: +XXX x xxx xxx, E-mail address: x.x@xxx.xx

[1] Organisation, Department, Address

[2] Organisation, Department, Address

Units and abbreviations: Required are SI units. Abbreviations must be given in text when first mentioned.

Proofreading: The proof will be send by e-mail to the corresponding author in MS Word's Track changes function. Corresponding author is required to make their proof corrections with accepting or rejecting the tracked changes in document and answer all open comments of proof reader. The corresponding author is responsible to introduce corrections of data in the paper. The Editors are not responsible for damage or loss of submitted text. Contributors are advised to keep copies of their texts, illustrations and all other materials.

The statements, opinions and data contained in this publication are solely those of the individual authors and not of the publisher and the Editors. Neither the publisher nor the Editors can accept any legal responsibility for errors that could appear during the process.

Copyright: Submissions of a publication article implies transfer of the copyright from the author(s) to the publisher upon acceptance of the paper. Accepted papers become the permanent property of "Journal of Energy Technology". All articles published in this journal are protected by copyright, which covers the exclusive rights to reproduce and distribute the article as well as all translation rights. No material can be published without written permission of the publisher.

Chapter examples:

1 MAIN CHAPTER

(Arial bold, 12pt, after paragraph 6pt space)

1.1 Section

(Arial bold, 11pt, after paragraph 6pt space)

1.1.1 Sub-section

(Arial bold, 10pt, after paragraph 6pt space)

Example of Equation (lined 2 cm from left margin, equation number in normal brackets (section. equation number), lined right margin, paragraph space 6pt before in after line):

Equation (1.1)

Tables should have a legend that includes the title of the table at the top of the table. Each table should be cited in the text.

Table legend example:

Table 1: *Name of the table (centred, on top of the table)*

Figures and images should be labelled sequentially numbered (Arabic numbers) and cited in the text – Fig.1 or Figure 1. The legend should be below the image, picture, photo or drawing.

Figure legend example:

Figure 1: *Name of the figure (centred, on bottom of figure, photo, or drawing)*

References

[1] **N. Surname:** *Title,* Journal Title, Vol., Iss., p.p., Year of Publication

[2] **N. Surname:** *Title,* Publisher, Year of Publication

[3] **N. Surname:** *Title* [online], Publisher or Journal Title, Vol., Iss., p.p., Year of Publication. Available: website (date accessed)

Examples:

[1] **J. Usenik**: *Mathematical model of the power supply system control*, Journal of Energy Technology, Vol. 2, Iss. 3, p.p. 29 – 46, 2009

[2] **J. J. DiStefano, A.R. Stubberud, I. J. Williams**: *Theory and Problems of Feedback and Control Systems*, McGraw-Hill Book Company, 1987

[3] **T. Žagar, L. Kegel:** *Preparation of National programme for SF and RW management taking into account the possible future evolution of ERDO* [online], Journal of Energy Technology, Vol. 9, Iss. 1, p.p. 39 – 50, 2016. Available: http://www.fe.um.si/images/jet /Volume 9_Issue1/03-JET_marec_2016-PREPARATION_OF_NATIONAL.pdf (7. 10. 2016)

Example of reference-1 citation: In text *[1],* text continue.

Nomenclature

(Symbols)	(Symbol meaning)
t	time

JET

JET I Journal of Energy Technology I Vol. 11, Issue 3, November 2018 I University of Maribor, Faculty of Energy Technology

ISSN 1855-5748

9 771855 574008